Since January 2020 Elsevier has created a COVID-19 resource centre with free information in English and Mandarin on the novel coronavirus COVID-19. The COVID-19 resource centre is hosted on Elsevier Connect, the company's public news and information website.

Journal of Colloid and Interface Science 619 (2022) 229–245

Contents lists available at ScienceDirect

Journal of Colloid and Interface Science

journal homepage: www.elsevier.com/locate/jcis

Pathways to community transmission of COVID–19 due to rapid evaporation of respiratory *virulets*

Mitali Basak [a], Shirsendu Mitra [b], Dipankar Bandyopadhyay [a,b,c,*]

[a] Centre for Nanotechnology, Indian Institute of Technology Guwahati, Assam 781039, India
[b] Department of Chemical Engineering, Indian Institute of Technology Guwahati, Assam 781039, India
[c] School of Health Sciences and Technology,Indian Institute of Technology Guwahati, Assam 781039, India

GRAPHICAL ABSTRACT

The motions of the virus laden respiratory droplets are studied to explore the spreading of viral infection. The role of evaporation guided bioaerosol formation for community transmission has been analyzed for the prediction of the waves of a viral pandemic.

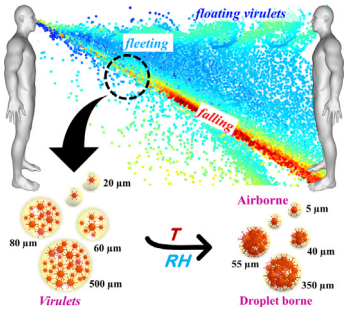

ARTICLE INFO

Article history:
Received 5 November 2021
Revised 6 March 2022
Accepted 21 March 2022
Available online 28 March 2022

Keywords:
COVID–19
Respiratory droplets
Viral load
Community transmission
Evaporation

ABSTRACT

Hypothesis: The formation of virus-laden colloidal respiratory microdroplets – the sneeze or cough *virulets* and their evaporation driven miniaturization in the open air are found to have a significant impact on the community transmission of COVID–19 pandemic.
Simulation details: We simulate the motions and trajectories of *virulets* by employing laminar fluid flow coupled with droplet tracing physics. A force field analysis has been included considering the gravity, drag, and inertial forces to unleash some of the finer features of *virulet* trajectories leading to the droplet and airborne transmissions of the virus. Furthermore, an analytical model corroborates temperature (*T*) and relative humidity (*RH*) controlled droplet miniaturization.
Results: The study elucidates that the tiny (1–50 μm) and intermediate (60–100 μm) size ranged *virulets* tend to form bioaerosol and facilitate an airborne transmission while the *virulets* of larger dimensions (300 to 500 μm) are more prone to gravity dominated droplet transmission. Subsequently, the mapping between the *T* and *RH* guided miniaturization of *virulets* with the COVID–19 cases for six different cities across the globe justifies the significant contribution of miniaturization-based bioaerosol formation for community transmission of the pandemic.

* Corresponding author at: Department of Chemical Engineering, Indian Institute of Technology Guwahati, Guwahati 781039, India.
E-mail address: dipban@iitg.ac.in (D. Bandyopadhyay).

https://doi.org/10.1016/j.jcis.2022.03.098
0021-9797/

1. Introduction

The recent outbreak of the deadly Severe-Acute-Respiratory-Syndrome Coronavirus 2 (SARS-CoV-2) pandemic has severely affected the health and economic conditions of the countries across the globe [1,2]. The use of face masks, maintenance of a healthy hand or face hygiene, and the use of a strict physical distancing protocol have become important practices for every individual to minimize the spreading of this highly contagious disease [3,4]. Importantly, it has now been scientifically established [5] that the pandemic spreads more rapidly through the micro/nanoscale airborne respiratory droplets, which emerge during the coughing, sneezing, breathing, or quiet/loud speeches of an infected individual [6,7]. This is because the viruses of ~100 nm diameter create a finely dispersed suspension with the mucosal fluid of respiratory tracts [8] and forceful breathing of air shears through the mucosal-air interface to generate the finely dispersed colloidal bioaerosol [9]. The size distribution of the colloidal microdroplets loaded with viruses is found to be in the range of 500 nm to a few hundred microns under varied conditions [10]. In that, the smaller ones have the tendency to spread the airborne infections while the bigger ones settle on the surfaces under gravity to spread the droplet-borne infections [13].

About a century ago, Flügge [11] in his seminal contribution demonstrated the concept of droplet transmission of infectious diseases such as malaria, tuberculosis, and cholera, which has been instrumental in the advocacy of Mikulicz-Radecki's for the surgical gauze masks [12]. In another path breaking contribution, Wells classified the airborne transmission after dichotomizing the respiratory droplets into larger and smaller varieties for tuberculosis [13]. Importantly, the transmission of other contagious diseases like tuberculosis, pneumonic plague, bronchitis, chicken pox, measles, or influenza also follow a similar transmission mechanism [5–7,14]. The droplet mode of transmission is possible when the virus loaded respiratory mucosal droplets are transported from the infected person directly to the exposed person or due to an indirect mode like a contact with the fomites of the infected person [15]. On the other hand, the airborne mode spreads through the exposure of virus-containing respiratory droplets in the air for a longer distance and for a longer period [15]. According to a recent report, the SARS-CoV-2 laden mucosal droplets oozing out from an individual forming bioaerosol [15] are among the prime reasons behind the community spread of the virus. The virus laden droplets then find their way to the healthy host through the angiotensin-converting enzyme-2 – ACE2 receptor protein located abundantly in the mucosae of conjunctiva and nose-epithelia causing serious respiratory disorders [16].

Interestingly, such fluid mechanical events are also very engaging from the perspectives of micro/nano droplet formation at the air-mucus interface and their transport through the air [17]. For example, smaller droplets may float in the air for a longer duration while even a mild air movement may transport the droplets further than usual [18]. Likewise, a smaller droplet may feel a much lesser gravitational pull while a bigger one may immediately precipitate after ensuing out of the nasal or mouth cavity. Importantly, the variation in the environmental temperature (T) and relative humidity (RH) in different geographical regions can play major roles in redefining the dynamics of the ejected droplets owing to the rapid evaporation and subsequent miniaturization. The dynamic change in the droplet diameter with these environmental parameters may transform a gravity-bound bigger droplet into an air bound floating droplet. Such miniaturized droplets are benefitted from deficit pull from gravity and can easily travel to longer distances packed with infectious viruses, which may trigger the community spread of the disease, as discussed in this article.

However, thus far, all the analyses and inferences related to the droplet and airborne modes of transmissions have been rather ad-hoc owing to a few important scientific and technological limitations: (i) the dynamic experimental imaging of the suspended coronavirus nanoparticle inside a moving droplet is a challenging task to achieve [19]; (ii) formation and transport of the mesoscale droplets of different size ranges from the nasal or mouth cavities are very difficult to characterize morphologically even with the state-of-art capacity of high-speed and high-resolution imaging [20]; (iii) the complexity is further elevated while tracking the viruses inside such droplet transport [21]; (iv) the relative humidity, temperature, level of pollutants, speed, and currents in air play crucial roles in the transport of the droplets [22]; and (v) size and angle of nose outlets, height of an individual, and the force of breathing, sneezing, and coughing are some of the parameters, which are very diverse across the globe [23]. Certainly, deeper scientific analysis and understanding of the fluid dynamics of the trajectory of the sneezed or coughed droplets is crucial to establishing a framework related to the physical distancing norms.

In this direction, one of the major scientific tools to explore the finer features of such a problem has been computational fluid dynamics (CFD) [24]. A number of prior seminal contributions have focused on exploiting the capacities of CFD to unearth the details of the respiratory droplet motion [25]. For example, Gupta et al. [26] have performed a benchmark to explore the probability distribution function mimicking the cough jets ejected by patients. Mittal et al. has summarized the generation mechanism of respiratory droplets and its parabolic flow physics governing the transmission of COVID-19 [27]. Xie et al. has reported a wide study of flow dynamics of respiratory droplets considering the turbulent flow of the cough jet considering effect of evaporation, relative humidity, air speed in a stagnant airflow for both water droplet and saline droplets [28]. Further, the effect of turbulence on the dispersion and deposition of the droplets in cough jets [29] and its exposure to close contact [30] has been explored in stagnant airflow conditions. The transmission of the respiratory droplets has also been analyzed in various closed environments like an elevator, supermarkets, classrooms equipped with partition, indoor conditions like an air-conditioned room or ventilated room, Intensive Care Units (ICU) as reported in various studies [28,31–35].

Apart from focusing only on the flow dynamics, the effects of various external factors affecting the transmission of respiratory droplets have also been explored broadly. The effects of atmospheric pollution [36], the viability of the 2 m of physical distancing norm [16,22,37], flow dynamics of a turbulent dry cough jet/puff having contagious pathogen [21], drying time of the respiratory droplets [19,38], the effect of evaporation time of droplets on infection transmission [39–41], and the effect of relative humidity and breakup of cough droplets on transmission intensity [16,22] have also been explored widely. Also, recently, the role of the size of water droplets [42] and the effect of evaporation of the water droplets [43] on the survival of the airborne viruses has been discussed. A very recent study uncover the flow dynamics of the ejected cough or sneeze droplets considering the movement of the head while sneezing [23]. The detailed study of Pendar [44] show a comprehensive examination of mild cough to intense sneezes considering various initial velocity, size distributions, injection angles of saliva micro-droplets and mouth-opening area along with different environmental factors that drive the transmission airflow inside a room. Also, Zhao et al. has shown that the droplets can travel three times farther in a wide range of temperature and humidity combination [45]. All these factors significantly characterize the aerosol based transmission of the disease attributing the second wave of COVID–19 [46].

The present study focuses on a rather unexplored topic wherein the viral loading and infection potency of the respiratory droplets

has been explored in detail to assess the risk of community transmission of SARS–CoV–2 infection. These respiratory droplets are the colloidal microdroplets of biofluid infused viral bodies – the sneeze or cough *virulets* which atomize into tiny bioaerosol to carry the loaded viruses faraway. Here, the spatiotemporal trajectories of the exhaled virus loaded droplets having various diameters have been simulated employing a complete set of fluid momentum equations and coupled fluid particle tracing physics. Moreover, the analyses of fluid flow fields and relative contributions of gravitational, drag, and inertial forces are quantitatively reported to strengthen the fundamental understanding of *virulet* dynamics. Furthermore, the effect of several sneezing or coughing frequencies and outdoor breeze conditions on the enhancement of dispersion of droplet transmission has also been reported.

Furthermore, remarkable observations have been unveiled to confirm the effect of *T* and *RH* mediated evaporation-driven on-the-fly miniaturization of the various sized *virulets* on the transmission of the infectious disease. Based on the *T* and *RH* data, the rate of miniaturization of the *virulets* has been analytically calculated for all six regions and has been mapped with the reported infection cases for the first wave of COVID-19 at that particular region. Interestingly, it was found that the trend in the rate of recurrence of the reported COVID-19 cases and their time resembles the mode of miniaturization of the *virulets* for the entire period for all the regions. In view of these observations, the evaporation model has been employed to predict the future occurrences of the infection waves and then compared with the reported infection cases including the second wave of COVID-19. The study shows that the predicted and the reported COVID-19 infection graphs proportionate well with a compromise of the intensity of the infection which may be attributed to the non-consideration of the additional causes of COVID-19 infection. Thus, the study unveils a strong relationship of the transmission of the disease in airborne mode with the rapidly evaporating microdroplets highlighting the fruitful novelty of the work. The most important part of the present work is drawing nonlinear correlations with statistical predictive models in R programming [47] for all the six cities. The correlation curves led to satisfactory *p* values indicating strong dependence of droplet miniaturization and COVID-19 infection. Further to this, the role of droplet flying, floating, and fleeting mediated by specific *T* and *RH* of that particular zone has been justified by CFD simulations with varying *T* and *RH*. For each zone, a demarcation line for *T* and *RH* has been drawn that signifies the onset of the high risk of COVID-19 transmission.

2. Theory

2.1. Problem formulation

Fig. 1 schematically shows the motion of respiratory droplets, ejected from an individual in the open air. The rectangular section in the figure shows the solution space, representing aerial premise of 3 m height (h) and 5 m length (l) in the proximity of the individual. The respiratory droplets enter into the solution space from inlets 1 and 2, which emulate the nose and mouth openings, respectively. In this regard, inlets 3 and 4 show the open-air inlets. Walls 1 and 2 represent the top and bottom boundaries taken sufficiently far from the nose inlet to represent the open air above and ground, respectively, while the outlet is assumed to be far away from the individual at a distance of 5 m, to study the extent of air-borne transmission. The position of the nose and mouth openings are placed at a certain height emulating the average height of an individual. The nose inlet has been tilted by an angle of 27°, which represents a downward motion while sneezing, as shown in the inset of the figure.

For the numerical modeling, a two-dimensional (2D) Cartesian coordinate system has been employed, which considers the effect of external airflow from inlets 3 and 4, on the motion of the expelled respiratory droplets of varied diameter (d). The fluid (air), in this model, is assumed to be isothermal, Newtonian, laminar, and incompressible. Further, for the droplets, the effect of evaporation has not been considered in the simulation. Additionally, the effect of the evaporated droplets has been incorporated by considering droplets of varying sizes. The horizontal and vertical directions are represented as x and y, respectively. A bold variable represents a vector and a variable in italics represents a scalar quantity. The scalar variables placed in the parenthesis of a vector indicate the components along the x and y directions. The velocity vectors of the fluid and droplets are symbolized as $\boldsymbol{u}_f(u, v)$ and $\boldsymbol{u}_d(u, v)$. The governing equations for the fluid flow are solved using the following continuity and Naiver-Stokes equations,

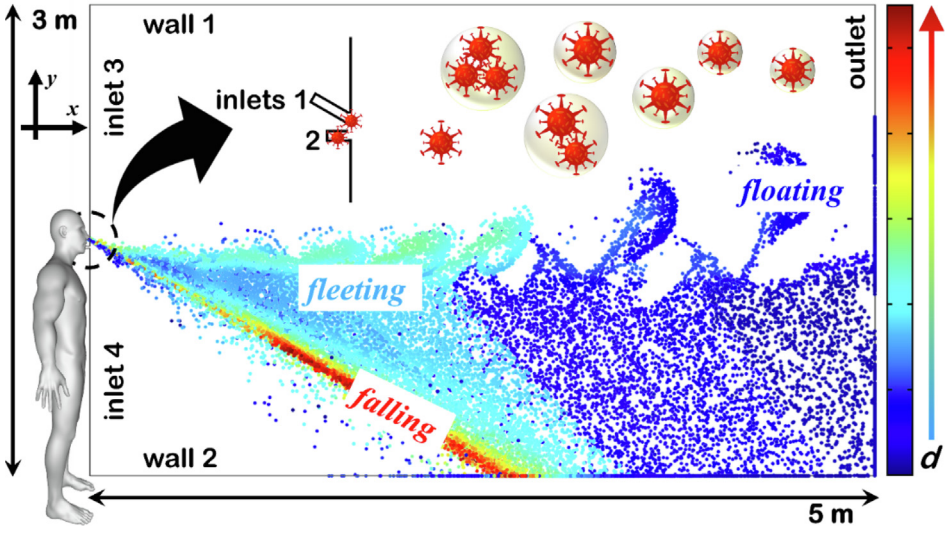

Fig. 1. Schematically shows the 2D geometry considered for the simulation study with the dimensions and axes. The nose and mouth openings are indicated as inlets 1 and 2, respectively while inlets 3 and 4 show the open-air inlets. The walls 1 and 2, at the top and bottom show the upper boundary and ground of the solution space, respectively while the outlet in the geometry is shown towards the right side. The respiratory *virulets* of varied diameter *d* have been indicated by different color code. The inset schematically shows the SARS-CoV-2 loaded respiratory droplets expelled from an infected person.

$$\nabla \cdot \boldsymbol{u}_f = 0 \tag{1}$$

$$\rho_f \frac{D\boldsymbol{u}_f}{Dt} = -\nabla p_f + \mu_f \nabla^2 \boldsymbol{u}_f + \rho_f \boldsymbol{g} \tag{2}$$

where ∇, D, p_f, μ_f, ρ_f, and g are the gradient operator, material derivative, air pressure, dynamic viscosity of air, density of air, and acceleration due to gravity vector, respectively. The motion of the droplets along with the external airflow has been modeled with the help of the following conservation of momentum equation,

$$\frac{\mathrm{d}(m_d \boldsymbol{u}_d)}{\mathrm{d}t} = \boldsymbol{F}_d^D + \boldsymbol{F}_d^g \tag{3}$$

where m_d is the mass of the droplet, $\boldsymbol{F}_d^D$ is the drag force, and $\boldsymbol{F}_d^g$ is the gravitational force experienced by the droplet. It has been observed that the sudden expelling of cough or sneeze droplets causes a transient high Reynolds number flow, which is impulsive [26]. However, the velocity of the droplets decreases with time and during its passage, it merges to a low Reynolds number laminar flow [48]. Hence, for this study, Stokes' drag [49], as shown in Eq. (4), has been employed for the droplets because the droplet Reynolds number for the different range are: 0.07 (1–50 μm), 1.50 (60–80 μm), and 5.56 (80–200 μm). For 300–500 μm, the Reynolds number is higher than 10, although well below the transition particle Reynolds number which is 500 [50]. However, the *virulets* in this range are significantly dominated by gravity, and do not tend to follow the fluid profile as discussed later.

$$\boldsymbol{F}_d^D = \left(\frac{18\mu_d}{\rho_d d^2}\right) m_d \boldsymbol{u}_r \tag{4}$$

Here, the notations, ρ_d, d, and μ_d are density, diameter, and dynamic viscosity of the droplet. Further, $\boldsymbol{u}_r = \boldsymbol{u}_d - \boldsymbol{u}_f$ represents the relative velocity of the moving droplet with respect to the velocity of the surrounding air. In addition, the gravitational force for the droplets has been considered employing the following expression,

$$\boldsymbol{F}_d^g = m_d \frac{\left(\rho_d - \rho_f\right)}{\rho_d} \boldsymbol{g} \tag{5}$$

2.2. Boundary conditions

To solve the Eqs. (1) and (2), no-slip and impermeable, $\boldsymbol{u}_f = 0$, boundary conditions are enforced on walls 1 and 2. The sneezing and coughing conditions are emulated using a Gaussian velocity distribution function at the inlets corresponding to nose and mouth with maximum speed, u_{m}, same as the speed of the sneezing or coughing, respectively. Table 1 depicts the function and the typical values that are employed for the simulations in the present study. The velocity boundary condition for the inflows at inlets 3 and 4 has been enforced as $\boldsymbol{u} = -u_0 \boldsymbol{n}$. The atmospheric pressure boundary condition $p = p_0$ is maintained at the outlet while the droplets are considered to be immovable after colliding the walls $\boldsymbol{u}_d = 0$.

Table 1
Shows the typical values for the parameters employed in the simulations.

Parameter/Expression	Values
Density of air, ρ_f	1 kg/m^3
Dynamic viscosity of fluid, μ_f	1.8×10^{-5} Pa s
Velocities at nose and mouth inlets, $u_{\mathrm{m}}(2\pi\sigma^2)^{-1/2} e^{-[(t-0.3)^2/(2s^2\sigma^2)]}$	u_{m} = 9.2 m/s for sneezing, u_{m} = 6.2 m/s for coughing, and $\sigma = 0.1$
Average air inflow, u_0	0, 1, 2 m/s
Droplet density, ρ_d	1200 kg/m^3
Droplet diameter, d_d	1–500 μm
Dynamic viscosity of droplet, μ_d	10^{-3} Pa s

3. Numerical simulation and validation

COMSOL™ Multiphysics, a finite element based CFD software, has been utilized for this work to solve the Eqs. (1–5) after enforcing the aforesaid boundary conditions. The software employs the Galerkin least-square method for the discretization of the equations with the boundary conditions and the fluid-particle-tracing (FPT) module has been employed for the droplet tracking in the surrounding air. In particular, the physics controlled unstructured triangular grids are used as the mesh elements during the simulations. For time marching, a backward difference scheme has been employed with an optimum time step of $\sim 10^{-4}$ s to obtain an accurate solution. Since the solution space is significantly large, 3 m × 5 m, as compared to the size of the droplets, 1–500 μm, a grid independence study is performed to satisfy the adequate mesh required for an accurate numerical solution. The **Table S1** of the **Electronic Supporting Information (ESI)** shows the details of the meshes, in particular number and size range, for four different cases, which are considered for the comparison. Further, the accuracy of the FPT module has been validated against a simple analytical solution and the simulation results obtained by Dbouk [22] are contrasted with the simulations from the proposed framework. The details of the mesh independence study and validation are shown in **Fig. S1** of the ESI.

4. Results and discussion

4.1. Viral load of Sneeze/Cough droplets

The respiratory processes like sneezing and coughing eject numerous water droplets with varying sizes ranging from less than 1 μm to 1000 μm in diameter or sometimes even larger [20]. These droplets are enriched with various elements like water, microbes, proteins, carbohydrates, or salts, apart from having different disease-causing agents like the SARS-CoV-2 virus. Since the focus of this work is to gauge the potency of these droplets in the transmission of viral diseases, these water droplets are termed as '*virulets*' in this script. The viral load (V_L) of a droplet ejected from a SARS-CoV-2 infected patient depends on his/her viral concentration (C_v) in the mucus. For example, asymptomatic to weakly infected patients have C_v in the range of $\sim 10^4$ copies/mL while severely infected patients may have as high as 10^9 copies/mL [51]. Thus, a droplet ejected from a patient can have a varied amount of viral load based on its size and the number of virus particles present inside the same. The probability of total viruses loaded inside a *virulet* for different C_v, can be approximated using Poisson's distribution [52] as,

$$f(n) = e^{-V_L d \frac{(V_L d)^n}{n!}} \tag{6}$$

Here, $f(n)$ is the probability of finding n number of viruses inside a *virulet* of diameter d, and $V_L(d)$ is the viral load,

$$V_L(d) = \frac{\pi}{6}\left(d^3 C_v\right) \tag{7}$$

In this study, d have been varied from 1 to 500 μm to consider the entire range of *virulet* sizes ejected during the respiratory activities like sneezing and coughing, and the size of the SARS-CoV-2 virus has been considered to be 100 nm in diameter, as reported elsewhere [53]. Fig. 2a shows the maximum number of viruses (n_{max}) that can coexist in a *virulet* of size d ranging from 1-500 μm for different C_v ranging from 10^4 to 10^9 copies/mL.

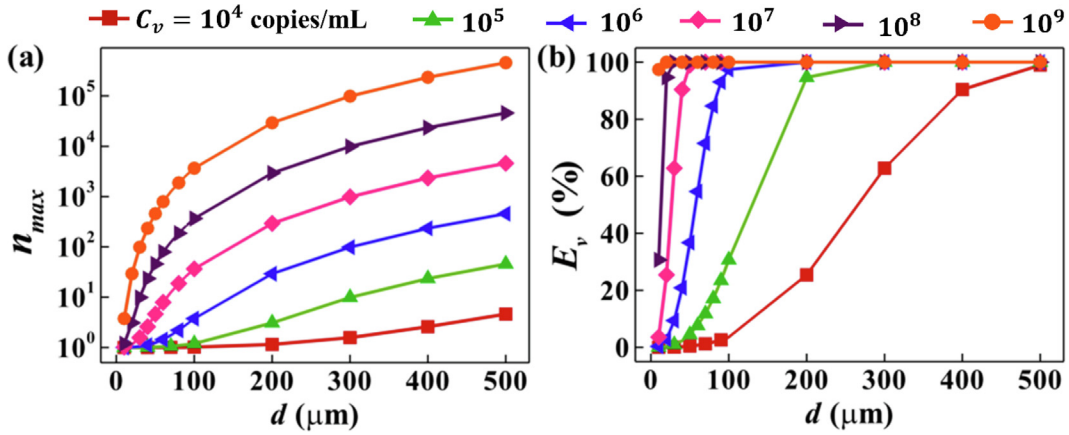

Fig. 2. Plot (a) shows the maximum number of viruses n_{max} loaded inside a droplet of size d ejected from an infected person, and plot (b) shows the fraction of E_v among the total droplets ejected of size d, for C_v ranging from 10^4 copies/mL to 10^9 copies/mL and d ranging from 1 to 500 μm.

The plots suggest that the n_{max} of an evicted droplet increases progressively with C_v. Considering a specific case, a 100 μm droplet can hold ~10 viruses for $C_v = 10^4$ copies/mL, however, the same droplet can hold ~6000 viruses when ejected from a patient with $C_v = 10^9$ copies/mL. In addition, a higher load of the virus is expected inside the *virulets* with a higher d. On the contrary, a bigger droplet with more viral load is expected to settle on the surface much faster while the smaller ones with a less viral load have the capacity to become airborne, as discussed later. The plots in the figure indicate that the infection potency of the *virulets* is less for smaller d (e.g. less than 100 μm) and lower C_v cases. However, such *virulets* may be of concern when expelled from a highly infected person.

The other important factor to note here is that all the *virulet* sneezed or coughed out may not be infectious. Fig. 2b shows the fraction of the effective number of *virulets* (E_v) among total number droplets ejected during sneezing or coughing. E_v can be defined as those specific droplets among all the expelled droplets which are loaded with viruses. Here, the total number of the ejected droplets is the total number of droplets of a specific size d that can be accommodated in 1 mL volume of water. The detailed calculation of E_v is given in **Section S2** of the **ESI**. The plots in Fig. 2 signify that for a lower C_v, a small fraction of the total ejected droplets are loaded with the viruses, whereas for a higher C_v, nearly all the ejected droplets can be filled with a significant number of viruses. For example, if 1 mL of water is transformed into its corresponding number of say d of 200 μm, then for C_v = 10^4 copies/mL, only ~22% of droplets host at least one virus. Conversely, for C_v = 10^9 copies/mL, each droplet (100%) may carry more than one virus during the ejection. The figure shows that for lower C_v, not all the droplets ejected are infectious. However, the majority of the droplets ejected from higher C_v patients are capable of spreading the disease. The plots also help in inferring that although the risk of infection of a healthy exposed person is high from droplets ejected from a higher C_v valued patient owing to higher n_{max} and E_v, the risk is not zero from asymptomatic or weakly infected patients.

4.2. Motion of respiratory virulets

In addition to the infection potency of the *virulets*, the infection risk of an exposed person also depends on the spatial distance of exposure from the infected person, i.e., the spreading distance of the *virulets*. Fig. 1 schematically shows the motion of the *virulets* ejected during a sneeze in different pathways for d of 1–500 μm – (i) *floating* in the air and traveling far away, (ii) *falling* to the ground at a shorter distance, and (iii) *fleeting virulets* traveling to an intermediate distance before sinking. Such different modes of transmission of the *virulets* are governed by their characteristic flow dynamics. Here, we have numerically simulated the micro *virulets* ejection of different size ranges through a human sneezing process and its subsequent spreading in the open air, as described in Fig. 3. In order to mimic the normal sneezing airflow, we consider a Gaussian velocity distribution function, as described in the previous section. In accordance with the common sneezing conditions reported by the previous study [54], the time of ejection of the droplets and maximum amplitude of the function are taken as 300 ms and 9.2 m/s, respectively. The Reynolds number calculated for the present system is found to be ~10^5 for 1 m/s external air condition and ~10^4 for 0.5 m/s, which is well below the turbulent transition limit of the open channel boundary layer system [55]. Also, we have compared the flow profile of the *virulets* for both 0.5 m/s and 1 m/s velocity conditions, as shown in Fig. S2 of **Section S3** of the **ESI**, and it illustrates no change in the motion of the *virulets* except the distance of spreading of the *virulets* which varies with the outdoor air velocity. Hence, the consideration of laminar flow is scientifically justified in the present system. Therefore, for all the calculations of the transmission of the droplets, as discussed later, the maximum air limit of laminar of 1 m/s has been imposed to study the spreading of the droplets.

For each range, 5000 number of *virulets* are taken to emulate the actual concentration during a human sneeze, and the same is at par with a previous study [54]. For all the simulation studies, external airflow is maintained at a light breeze of 1 m/s, moving from the left of the solution space to the right, maintaining a laminar flow. The flow profiles of such systems have been simulated for different-sized droplets for a time period of 5 s. A set of four droplet size ranges is considered to review the landing trajectory and flow velocities at different time periods until 5 s. The typical droplet size ranges taken are, 1–50 μm, 60–80 μm, 80–200 μm, and 300–500 μm, as shown in the Fig. 3a–d and **Supporting Video 1** of **ESI**. The color bar in Fig. 3d represents the corresponding size of the *virulets* considered for the study. Fig. 3e–h show temporal variations of the x and y-directional velocities of 1–50 μm, 60–80 μm, 80–200 μm, and 300–500 μm sized *virulets*, respectively.

Fig. 3a shows the flow trajectory of 1–50 μm sized *virulets*, which suggests that these *virulets* are likely to travel a longer distance, larger than 5 m in 5 s time following a re-circulatory flow pattern, as can be found in the image set of Fig. 4a. Interestingly, the *virulets* form trajectories resembling the rotating fluid vortices, when they float in the air. Fig. 3e suggests that the x-directional

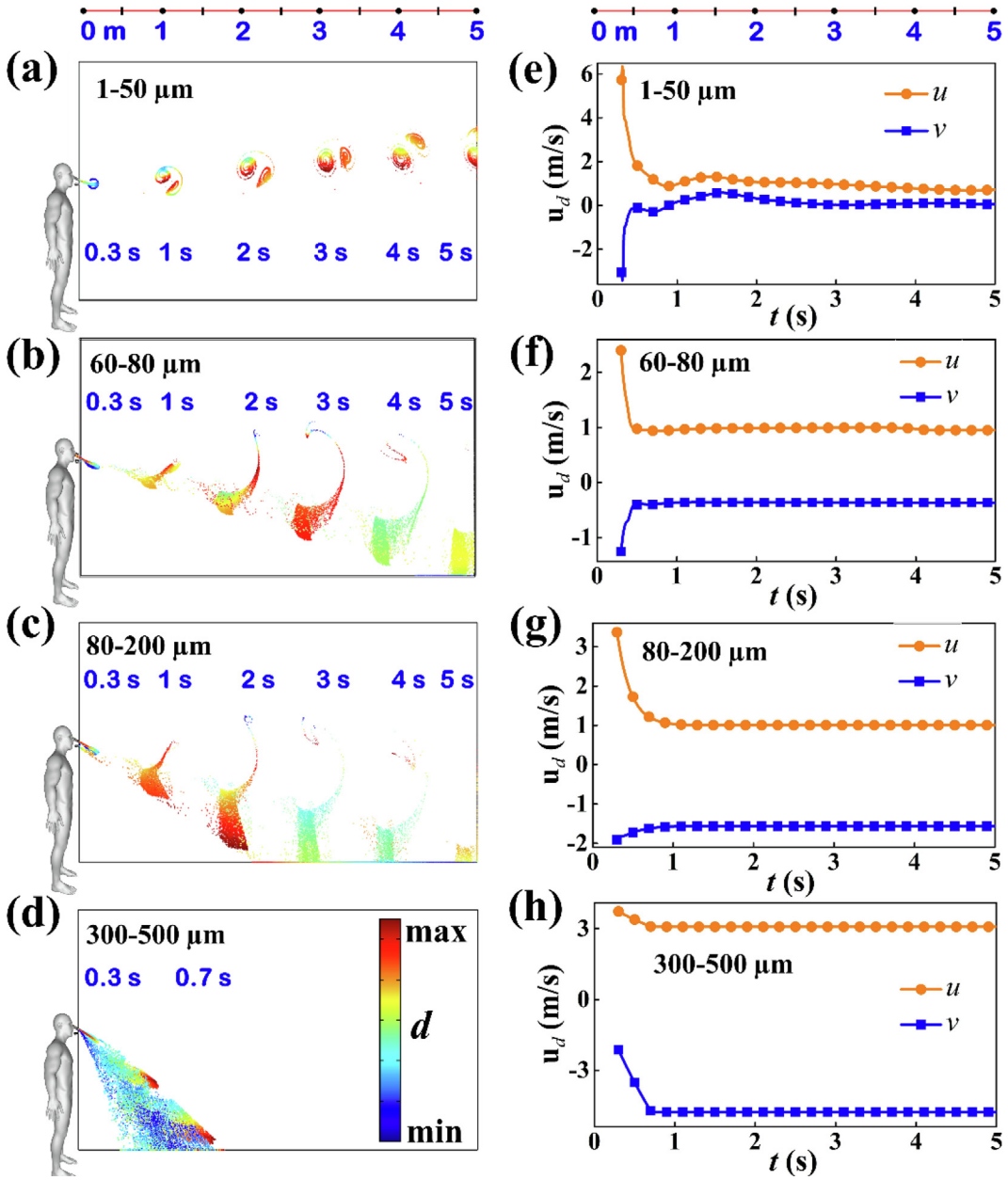

Fig. 3. Plots (a) – (d) show the flight trajectory and (e) – (h) shows the corresponding velocity profiles of the *virulets* expelled from the sneeze of a SARS-CoV-2 infected person, taking droplet size ranges of 1–50 µm, 60–80 µm, 80–200 µm, 300–500 µm, respectively. The color bar in subplot (d) shows the dimension range of the simulated *virulets*, the terms 'min' and 'max' indicate minimum *virulet* diameter and the maximum *virulet* diameter of that droplet range, as considered in subplots (a–d).

velocity, u, of the *virulets* is maximum at the nose inlet (at 0.3 s), which reduces progressively with the time and distance traveled. On the other hand, the y-directional velocity of the *virulets*, v, is towards the ground (less than 0) during the ejection. With the progress in time, the *virulets* become air bound as v increases with time. The figures together suggest that these tiny *virulets* drift in a forward direction from the inlet and drive upwards during its pathway with an increase in v, and do not settle to the ground easily. Therefore, the *virulets* in this range remain suspended in the air for a long time and can transit to a far distance with the airflow. The ejection of fluid into the computation domain develops local counter rotating twin vortices in the nearby space, as shown in Fig. 4.

Such local wakes infused with *virulets* are convected further by the laminar flow of the surrounding fluid. However, the *virulets* to follow the fluid vortices are decided by the forces acting on it – inertia, drag, and gravity force. The smaller droplets by virtue of inertia tend to float along with the fluid vortices mimicking the circulations, which lifts the tiny droplets to travel to long distances, as shown in Fig. 4a. The detailed analysis of the forces acting on the virulets is discussed further in the script.

Fig. 3b shows the trajectory of the 60–80 µm sized virulets and the corresponding temporal variations of the x- and y-directional velocities are shown in Fig. 3f. Fig. 3b suggests that the spreading distance of these *virulets* after 5 s is relatively smaller than in 3a. The figure also shows that the bigger *virulets* in the range settle on the ground at a much shorter distance while the smaller ones can still become air borne within 5 m. Again, Fig. 3f shows a positive v at the downstream indicating an upward drift for the smaller *virulets* in the range, following the rotation of the fluid vortices, as portrayed in Fig. 4b. Fig. 4b also illustrates that the bigger *virulets* in the 60–80 µm range depart from the vortex street, after a while, towards the downstream. This is due to the dominance of gravity on the bigger *virulets* governing its trajectory over the course of

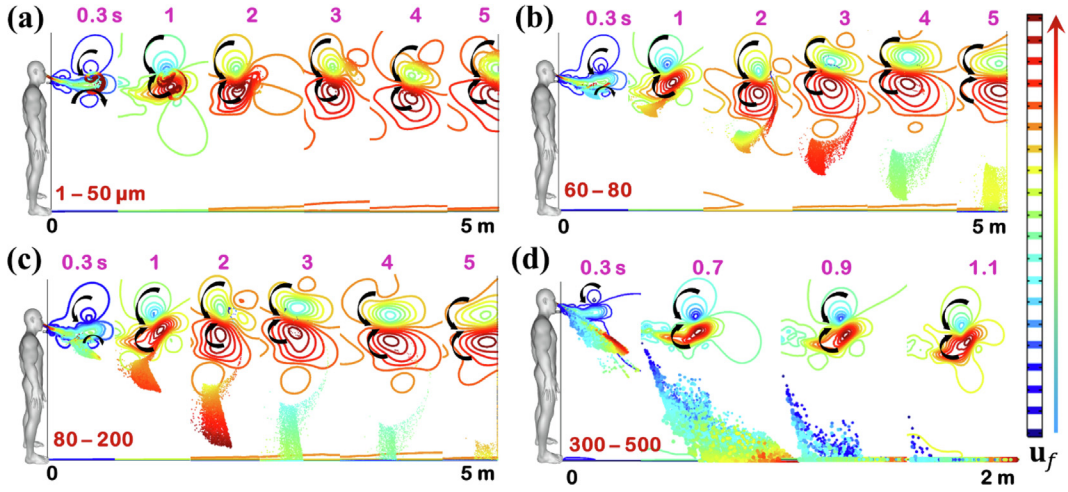

Fig. 4. Image sets show the velocity contour of the *virulets* sized (a) 1–50 μm, (b) 60−80 μm, (c) 80–200 μm, (d) 300–500 μm.

time. Similarly, the motions of 80–200 μm sized *virulets*, as shown in Fig. 3c**,** illustrate that the *virulets* settle to the ground at a much shorter time as compared to the prior two cases.

The corresponding velocity profiles in Fig. 3g also suggest a substantial downward motion of the *virulets*. Unlike the prior two cases, these *virulets* shed from vortex street and move away to the downstream rapidly, as shown in Fig. 4c, whereas the smaller ones followed the fluid vortices. Interestingly, with a further increase in the size to 300–500 μm, the *virulets* settle to the ground within a second of the ejection, as can be found in Fig. 3d. Fig. 4d also shows that the *virulets* escape the fluid vortices and settle to the ground immediately after ejection from the nose. The corresponding velocity profiles in Fig. 3h also confirm the sharp decline in u and v within a short time.

Concisely, the simulations suggest that, with an increase in the *virulet* size from 1–50 μm to 300–500 μm, the settling distance decreases from more than ∼5 m in 5 s to less than 1.5 m in ∼1 s, respectively. The flow trajectory of the *virulets* ejected during coughing is illustrated in **Fig. S3 in section S4** and **Supporting video 2** of the **ESI**. The simulations help in differentiating the *floating virulets* to be with $d < 70$ μm, *fleeting* to be with 70 μm $\leq d \leq$ 200 μm, and *falling* to be $d >$ 200 μm. Remarkably, the simulations suggest that they can travel a much larger distance than the standard protocol of 2 m set for physical distancing and can be one of the major reasons behind the community transmission with the high viral potency. In this regard, one may easily envision that the *floating virulets* may exclusively adopt the airborne mode of disease transmission while the *falling* ones may facilitate droplet or fomites mode of disease transmission. The *fleeting* mode may contribute towards both the modes. The images in Fig. 3 also illustrate that an exposed person at a similar height or more than the infected one is vulnerable to the passing *virulets* even at a distance of greater than 2 m when the *virulets* are airborne. However, the children are more susceptible to the *virulets* even at the close vicinity of the infected person through the falling *virulets*. Moreover, the *floating* respiratory droplets ejected from an infected child can be sufficiently active to transmit infections to the adults through the air borne recirculation of the *virulets*.

4.3. Analyses of force fields acting on virulets

Detailed understanding of the droplet dynamics coming out of patients' nose or mouth is crucial to foresee the infectivity potential of these *virulets*. The *virulets* ejected during a sneeze, form a conical jet near the nose inlet and are mostly affected by the inertia force and thus travel along the direction of the initial velocity. As the *virulets* travel far from the nose inlet, the droplet velocity, $\boldsymbol{u}_d$, coupled to the surrounding fluid velocity, $\boldsymbol{u}_f$, decreases progressively from its maxima, as described earlier. The *virulets* in this regime experience a swirling flow during the motion due to the shearing of the ejected conical jet in the calm air around the inlet of the solution space [56]. As the particles move further, the size of the *virulets* determines their destination, as depicted in Fig. 5. The component-wise force analyses along the normal directions of the Cartesian reference frame are done to explore the finer features of virulet dynamics. The trajectory of the *virulets* is mostly governed by three major factors – ejection inertia, downward gravitational pull, and viscous drag. Since the study is done employing *virulets* of a varying size range, the contribution of different forces alters with subsequent changes in its trajectories.

Fig. 5a and Fig. 5b show drag force acting in horizontal (x–axis) and vertical (y–axis) directions, respectively, for different sized particles. In addition, Fig. 5c and Fig. 5d show the inertial forces in horizontal (x–axis) and vertical (y–axis) directions, respectively. The domination of gravitational pull with size can be substantiated from Fig. 5e. For 1–50 μm sized *virulets*, on comparing the two x-directional forces, i.e. F_d^{Dx} acting along the negative x-direction and F_d^{Ix} acting along the positive x-direction, it can be observed that the inertia of the *virulets* is relatively much higher than its drag force. Thus, the act of inertia is responsible for the faraway forward motion of these tiny *virulets*. Comparing all the y-directional forces, i.e. F_d^{Dy} acting in the upward y-direction, and F_d^{Iy} and F_d^{g} acting along the negative y-direction, it can be inferred that the act of gravity is relatively very small due to smaller size, and an act of inertia is very less due to lesser mass as compared to the drag force. Thus, the effective drag force in positive y-direction causes the lift of the *virulets* in the upward direction.

Similar observations can be made for 60 − 80 μm sized *virulets*, which causes the lift and forward motion. However, the effectiveness of the resultant x and y directional forces for 60–80 μm sized *virulets* are relatively minor than for 1–50 μm, which causes them to settle earlier. Comparing the x-directional forces for 80–200 μm and 300–500 μm sized *virulets*, the inertial force is comparatively smaller than its drag force along the x-direction. Also, the combined forces of gravity and inertia along negative y-direction are higher than the upward drag force. Due to higher gravitational and inertial act along the downward direction, these *virulets* tend to settle much faster as compared to the 1–50 μm and 60–80 μm sized *virulets*. Of course, the resultant action of the x and y direc-

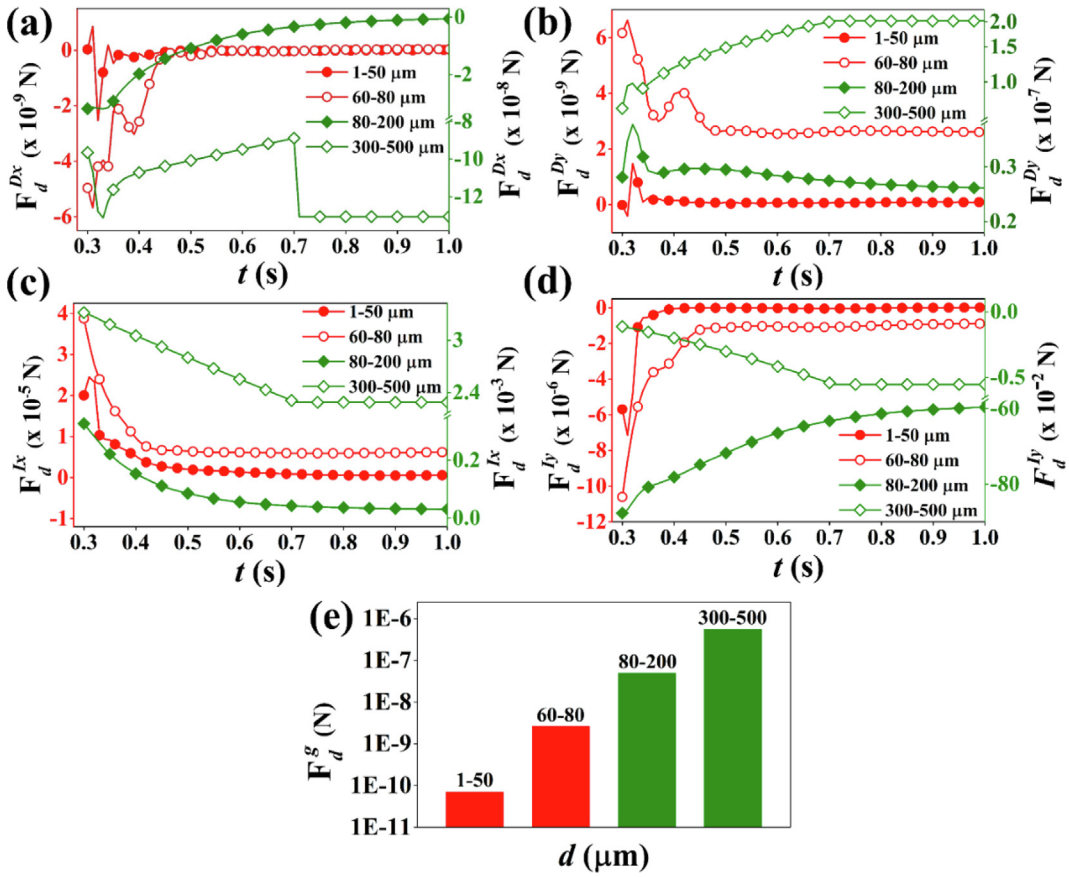

Fig. 5. Plots (a) to (e) show the x – directional drag force (F_d^{Dx}), y – directional drag force (F_d^{Dy}), x – directional inertia force (F_d^{Ix}), and negative y – directional inertia force (F_d^{Iy}), and negative gravitational force (F_d^g) acting on the particles of size ranges of 1–50 μm, 60–80 μm, 80–200 μm, 300–500 μm, ejected via sneezing.

tional forces is higher for 300–500 μm sized *virulets* owing to larger size and mass than for 80–200 μm, which explains the immediate fall of the 300–500 μm sized *virulets* after ejection as for 80–200 μm *virulets*.

In order to further explore the flow dynamics of the *virulets*, Froude's number (*Fr*), Reynolds number (Re_p), Weber number (*We*), and Capillary number (*Ca*) has been calculated for the *virulets* of size ranges of 1–50 μm, 60–80 μm, 80–200 μm, 300–500 μm, ejected via sneezing, for the time period of 5 s, as shown in Fig. 6a–6d. Fig. 6a shows that the smallest *virulets* of 1–50 μm size experience higher *Fr* owing to its high inertia and low gravity and with an increase in *virulet* size to 300–500 μm, the *Fr* decreases gradually. This is because the gravitational force acting on the *virulets* of larger *virulets* increases with an increase in size as shown in Fig. 5. Here, the floating *virulets* of 1–50 μm size shows an oscillatory behavior of the *Fr* during its course of the flow which is mainly because of the variation in the velocity of the *virulets* at a particular time owing to various forces acting on it as described in Fig. 3 and Fig. 5. Fig. 6b shows the Re_p increases with an increase in the diameter and velocity of the *virulets* at a given location. However, Re_p for all the *virulets* size is well below the turbulent limit of 500 [50] which shows the consideration of laminar is valid in the present study. Similarly, *We* and *Ca* shown in Fig. 6c and Fig. 6d, respectively, show that the spherical liquid bubbles do not deform during their motion in the external wind.

4.4. Effects of multiple ejections and wind flow

Further, the infectivity risk from the traversing *virulets* can also augment by frequent medical factors like simultaneous sneezing and coughing by the infected person, heightened coughing or sneezing frequency, or by external influences like a windy day. The effect of these factors on the spreading of the *virulets* is depicted in Fig. 7. The motion of infected respiratory *virulets* in case of simultaneous sneezing and coughing from an infected person is shown in Fig. 7a and Fig. 7b and in **Supporting Video 3** of the **ESI**. A range of 1–500 μm sized droplets, expelled from the nose or mouth of an infected person with velocities same as for single sneezing or coughing processes has been considered for the study. It can be easily inferred from the figure that the density of the *virulets* in the given area is more during simultaneous sneezing and coughing process as compared to single sneezing or single coughing processes with an increase in the time lag between the two processes from 0.1 s to 0.4 s, although the trajectory of motion remains the same. The more the *virulets* are expelled by the infected person, the more is the risk of the spread of the infection. Another such event of enrichment of infected droplets in a given area could be multiple ejections of the infected respiratory droplets, by an infected person.

Fig. 7c **and** Fig. 7d and **Supporting Video 4** of the **ESI** highlight the droplet trajectories and the increase in density of the *virulets* in case of multiple sneezing from a single sneeze to four times simultaneous sneezing. It can be depicted from the figure that with the increase in the sneezing frequency, the density of the *virulets* also increases in the given area. Consequently, anyone, irrespective of the height, exposed to the infected person's vicinity is at higher risk of inhalation of the expelled *virulets* and thus getting infected with the disease.

Additionally, the external wind conditions can also augment the spreading of the *virulets*. The effect of the external wind speed on

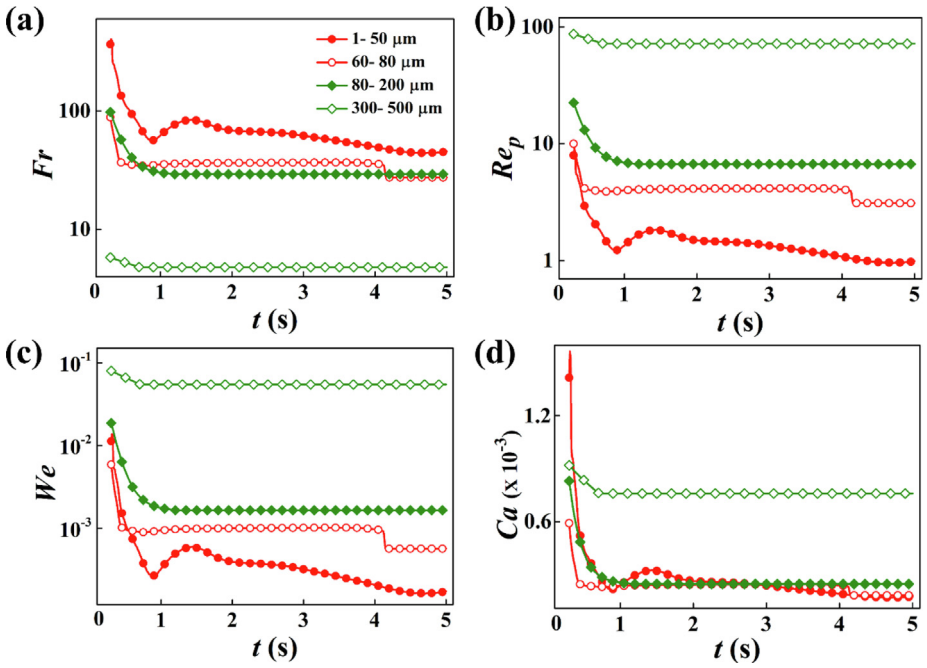

Fig. 6. Plots (a–d) show the Froude number, Reynolds number, Weber number, and Capillary number for the *virulets* of size ranges of 1–50 μm, 60–80 μm, 80–200 μm, 300–500 μm, ejected via sneezing, respectively.

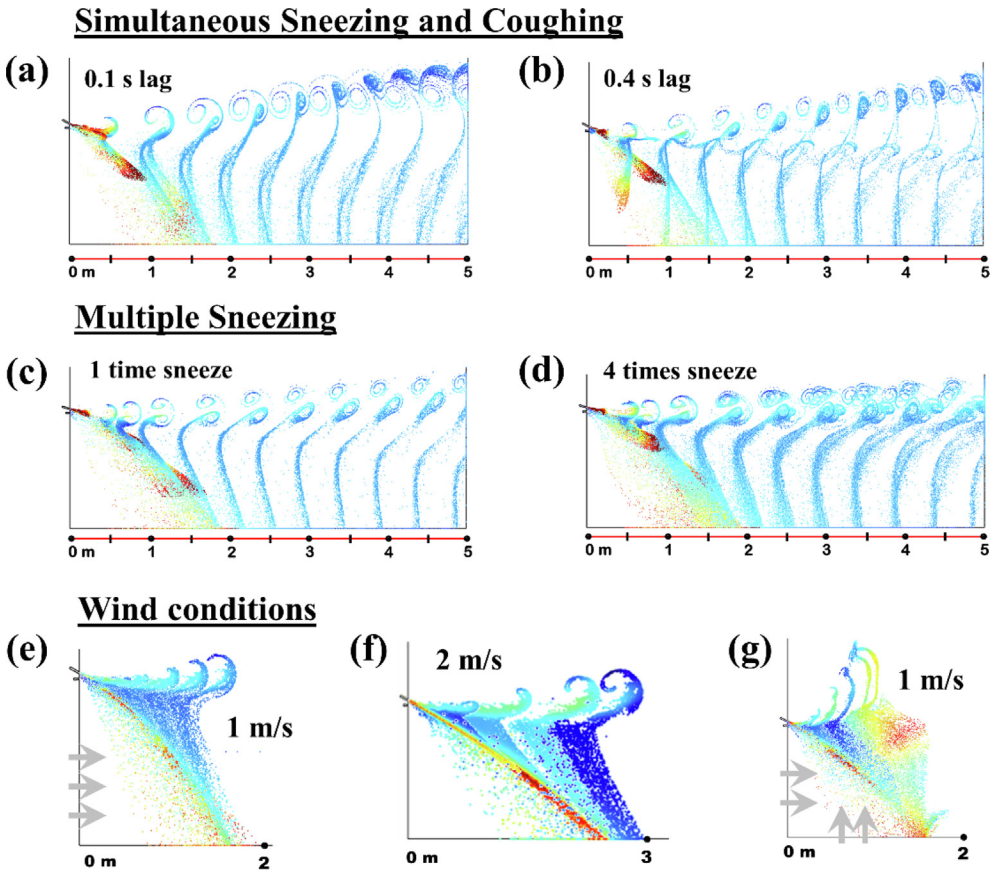

Fig. 7. Shows different events that enhances the transmission of SARS-CoV-2 *virulets*, enhancing the community spreading of the disease. Plot (a) shows the spreading of *virulets* ejected during simultaneous sneezing and coughing from a SARS – CoV – 2 infected patient with time lag between the two events be 0.1 s and (b) 0.4 s. Plot (c) shows the distribution of *virulets* during single sneezing and (d) sneezing for 4 times. Plot (e) shows the dispersal of the *virulets* during external wind conditions of light breeze of 1 m/s from left to right, (f) moderate breeze of 2 m/s blowing from left to right , and (g) light breeze of 1 m/s from left to right and botton to up of the solution space, respectively. The time frames from 0.3 s to 5 s has been combined in one image for all the cases.

the spreading distance of the respiratory *virulets* is illustrated in Fig. 7e–g and in **Supporting Video 5** of the **ESI**. Three different external wind speed conditions, light breeze (1 m/s) and moderate breeze (2 m/s) from left to right of the solution space, and an angular light breeze (1 m/s) from left to right and bottom to top are considered for the analyses for 1 s time for *virulets* ranging from 1–500 μm. It can be observed that under light breeze conditions of 1 m/s, Fig. 7e, the *virulets* do not traverse more than 2 m distance in 1 s time whereas it is 3 m for 2 m/s, shown in Fig. 7f. In the case of angular breeze condition, Fig. 7g, the aerial transmission of the ejected *virulets* is amplified by the external breeze. Consequently, the natural pathways may also play an important role in the community transmission of the disease.

4.5. Effect of temperature and relative humidity on virulet evaporation

The spreading of the *virulets* is a major factor in the community transmission of SARS – CoV – 2, which depends on how remote the respiratory droplets can travel carrying the infection causing agents. The time of fall of the *virulets* termed as settling time (t_s) decides how long it can survive freely before dropping to the ground. t_s of a *virulet* can be obtained by balancing the Stroke's friction force with the $\boldsymbol{F}_d^g$ experienced by the *virulets* during its flow [41], as given in Eq (8),

$$t_s = \frac{h}{V_s} \tag{8}$$

Here h is the height at which *virulets* are ejected which is the height of the infected person – 1.5 m in this case, and V_s is the velocity of the virulet of radius R_0 at the time of fall – the settling velocity, given by.

$$V_s = 1.2 \times 10^8 \left(R_0^2\right) \tag{9}$$

Remarkably, t_s of the *virulets* alters during its flight due to the modification in its size (R_0) owing to surrounding weather conditions such as T and RH. The variations in T and RH stimulate the miniaturization of the traversing *virulets* by virtue of evaporation. Accordingly, from Eq. (8), the reduction in R_0 enhances the t_s and hence the *virulets* can flow with air for a longer time before falling to the ground and spread faraway aiding the community transmission of the disease.

Fig. 8a schematically shows the miniaturization of the ejected *virulets* to the evaporated *virulets* at $T = 25\ ^\circ$C and $RH = 50\%$. It can be observed from the figure that the diameter of the ejected droplets can change from the *falling* to the *floating* ones owing to the evaporation followed by miniaturization of the size. Such miniaturization increases the infection potency because, as discussed in Fig. 2, the bigger droplets always carry a larger number of viruses, although they tend to settle easily on the surface under gravitational pull. However, if the T and RH of the surroundings facilitate the floating of such falling *virulets* due to rapid evaporation, the droplets with more virus loading may become air borne with a more potency towards the viral transmission. Further, the miniaturization of the ejected droplets also depends on the number of viruses loaded inside that droplet. If we assume the complete evaporation of an ejected droplet to be a state at which all the water content of the ejected droplet vanishes, then the miniaturized size of that ejected droplet is equivalent to the diameter corresponding to the total volume of all the viruses contained in that particular droplet.

Fig. 8b shows the minimum possible diameter of the *virulets* after complete evaporation, d_e, for different C_v ranging from 10^6 to 10^9 copies/mL. For example, say for $C_v = 10^6$ copies/mL, a droplet of 100 μm can hold a maximum of 400 viruses, as can be found in Fig. 2. After complete evaporation, the minimum possible miniaturized droplet size, $d_e = 155$ nm, which is the equivalent diameter to the volume of 400 number of 100 nm sized viruses loaded inside a 100 μm sized ejected droplet for $C_v = 10^6$ copies/mL. However, the evaporation and subsequent state of miniaturization of d to d_e depends on t_s, as described in Fig. 8c.

Fig. 8c shows a comparison of the evaporation time (t_{eva}) of d,t_s and the settling time of the miniaturized droplets (t_e) after evaporation. It can be observed from the plot that for d less than 80 μm, t_s is substantially larger than the t_{eva}. This means the *virulets* get adequate time to evaporate before settling to the ground and thus these *virulets* are capable to reach its d_e at its corresponding t_{eva}. For d ranging from 80 μm to 200 μm, t_s is comparable to t_{eva} and thus the evaporation fate of these *virulets* to reach d_e depends on the external T and RH conditions. However, for d greater than 200 μm, t_s is very less than t_{eva}, which means that the *virulets* will not get sufficient time to evaporate much and will settle to the ground immediately after ejection. In addition, t_e is found to be in the order of several days as shown in Fig. 8c, which emphasizes that the evaporated *virulets* that form the *floating* miniaturized droplets are the bioaerosols that can suspend and circulate in air for days before falling down. The calculations for determining t_{eva} and d_e is given in **Section S5** of the **ESI**.

Seemingly, it is evident from the results shown above that the effect of evaporation plays a significant role in the spreading of viral infections via *virulets*, which are also highlighted in the past literature [41]. In a tropical country like India, the climatic conditions relative to T and RH varies across the geography. The western regions experience high temperatures up to $T = 50\ ^\circ$C whereas the eastern regions experience cold weather throughout the year, and the coastal regions experience high humidity as compared to the other states. Similarly, the climatic conditions of different countries across the globe also vary during different seasons throughout the year. These variations in the T and RH decides the rate of the evaporation of the *virulets* in a particular region and at a particular time of the year. Thus, the rate of the miniaturization of the *virulets* to evolve into bioaerosol also varies with geographic location and seasonal changes.

Fig. 9 represents schematically the effect of change in the T and RH on the miniaturization of 100 μm sized *virulet* for various T and RH conditions. The figure shows that for $T = 40\ ^\circ$C and $RH = 10\%$, the 100 μm can miniaturize to 1.1 μm in just 2 s whereas, for $T = 40\ ^\circ$C and $RH = 40\%$, the *virulet* evolve to 6.24 μm in 4.5 s. Similarly, for cold conditions, like for $T = 10\ ^\circ$C and $RH = 10\%$, the *virulet* evolves to approximately half of its size in 4.5 s and for $T = 27\ ^\circ$C and $RH = 95\%$, the miniaturization is minimum i.e. 77.43 μm in 5 s. Thus, the figure illustrates that the hottest and low to moderate humid conditions suffer the fastest bioaerosol formation.

4.6. Comparison of COVID-19 infection and virulet evaporation

The transmission of COVID–19 in a particular region depends on a number of crucial factors like the density of population [57], genetic makeup [58] and age of the people [59], metabolic comorbidities [60], healthcare facilities [61], lifestyle factors of hygiene [62] and diet [63], susceptibility of the exposed person [64], administrative control [65], climatic conditions of the region [66], mutation of the virus [67], vaccination rate [68] and among others. Of all the factors listed one of the major causes of the bioaerosol formation is the meteorological conditions of a location that has been accredited to the occurrence of the highly infectious second wave of SARS-CoV-2 pandemic. A number of recent studies have been performed to study the possibility of the airborne transmission of the infection. In one study, authors have detected the presence of SARS-CoV-2 ribonucleic acid in the air samples col-

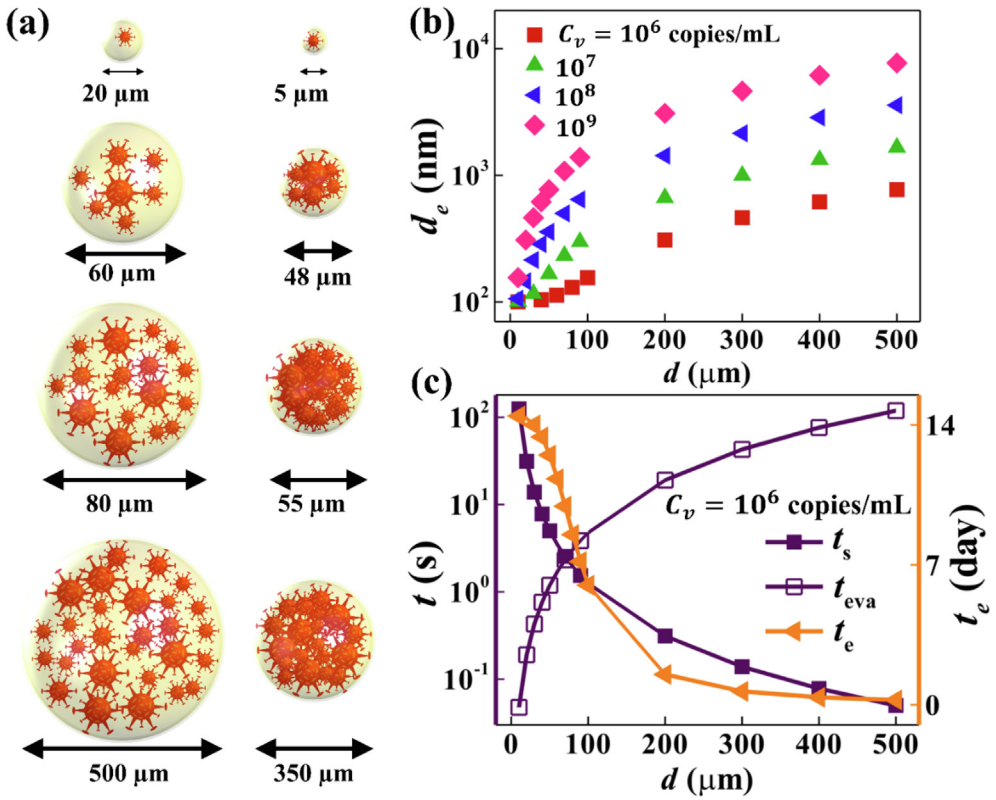

Fig. 8. Shows the effect of evaporation on the *virulets*. Plot (a) schematically shows the miniaturization of the *virulets* at $T = 25\ ^{\circ}C$ and $RH = 50\%$. Plot (b) shows the minimum possible d_e that an ejected droplet d can achieve after complete evaporation for different C_v ranging from 10^6 to 10^9 copies/mL. Plot (c) shows the comparison of t_s, t_{eva}, and t_e for $C_v = 10^6$ copies/mL.

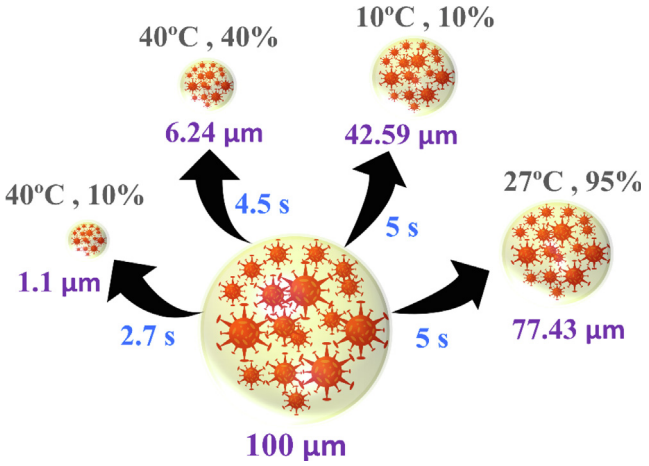

Fig. 9. Schematically shows the effect of evaporation due to variation in T (in °C) and RH (in %) conditions on a 100 µm sized *virulet*.

lected from various regions, with successfully cultured virus from a few samples. Along with that, they have also reported that SARS-CoV-2 is viable in artificially generated aerosols [69]. Another study also reports the presence of SARS-CoV-2 virus in air collected from both indoor and outdoor environments [70]. In another study, the evidence of airborne transmission of the disease has been proved in a church singing event in Australia. It was found that the secondary case patients were seated in approximately 15 m proximity of the primary patients without close physical contacts, suggesting air as the mode of the transmission of the disease [71]. Apart from these, epidemiologists have also reported the airborne transmission of the virus and the low air humidity as the most possible reason for the rapid spread of the disease in the Amazonian states [72]. Moreover, other than SARS-CoV-2, air borne transmission of other diseases like tuberculosis, streptococci, pneumococci, coliform organisms, and influenza virus has already been reported for long time [73–76]. In view of this, we have voluntarily opted to map the effect of evaporation of the ejected respiratory droplets as an effect of external T and RH with the trend in the increase in infection rate at different geographical regions.

In this section, we focus on comparing two sets of parameters based on the T and RH conditions to understand such community transmission of the *virulets*. In the first set, we investigate the correlation between the evaporation driven rates of miniaturization of virulent (dm^R/dt) with the rate of occurrence of confirmed cases of COVID–19 $\left(di^R/dt\right)$. As a second case study, we show the correlation of evaporation rate (m) and the absolute number of confirmed cases (i). The entire comparison analyses are made considering the three most COVID–19 infected places, Maharashtra, Karnataka, and Delhi, from India and three major cities across the globe, Los Angeles, São Paulo, and Paris. The study is envisioned to predict the future occurrence of COVID–19 waves based on the T and RH of the various places across the globe. The data for the number of confirmed cases of COVID–19 infection have been collected from two authentic websites; (i) https://www.covid19india.org/ for Indian regions, and (ii) https://www.worldometers.info/ for the world data. The rate of miniaturization of the *virulet* in the air due to evaporation has been calculated from Eq. (10), given by Williamson and Threadgill [77],

$$\frac{dd}{dt} = \frac{-4M_L D_v f}{d\rho_L RT}\Delta P\left(1 + 0.276R_e^{0.5}S_c^{1/3}\right) \tag{10}$$

Here, M_L, ρ_L, T, $D_{v,f}$, R , Δp, Re and Sc are the molecular weight of water, the density of water, average absolute temperature, the average diffusion coefficient for vapor molecules at T, gas constant, the difference between the vapor pressure near d and that in the ambient atmosphere, Reynolds number, and Schmidt number, respectively. The T and RH data for the calculation are collected from the meteorological website, https://www.timeanddate.com/, for the respective date on which confirmed cases have been taken for the study. The T and RH data used for the study are provided date-wise in section **S6** of the **ESI**.

It may be noted here that the parameters we are exploring in this study are not the only factors for the spreading of the pandemic. There are other multiple scientific, mutational, physiological, environmental, and administrative factors that determine the spreading of the infection. However, despite having the influence of such parameters, we observe a very faithful correlation between $\left(\mathrm{d}i^R/\mathrm{d}t\right)$ and $(\mathrm{d}m^R/\mathrm{d}t)$.

Fig. 10a–f show the case study for three major COVID–19 affected regions in India – Maharashtra, Karnataka, and New Delhi, respectively. Fig. 10a shows the rate of miniaturization of the ejected droplets and the rate of change of confirmed COVID–19 cases against different dates counted from June 2020 to June 2021 to study the first and second waves. It should be noted here that the dates considered for the study are in accordance with the rising of first and second COVID–19waves at that particular location. It is evident from the figure that the trend of matches fairly with. The plots also show a time lag between the rate of infection and the rate of miniaturization of the droplets. Intuitively, one can easily envisage that this lag is correlated to the formation of bioaerosol first and then the spreading of the infection leading to the increase in the cases. In a way, such an observation justifies the possibility of the formation of bioaerosol due to the variation in T and RH at different times of the year and in different regions.

In a different case analysis, Fig. 10b shows the comparison of occurrence of COVID–19 cases i and the evaporation rate of the droplets m. It can be seen from the figure that in this case too, the trend in the increase in COVID–19 infection is comparable with the evaporation rate curve. The dotted curves are the extrapolated arches of the rise in COVID–19 cases in accordance with the evaporation rate calculated from July 2021 to December 2021, as discussed later. Fig. 10c and Fig. 10d show similar analyses for Karnataka, and Fig. 10e and Fig. 10f show analyses for Delhi. These cities show a very similar trend of infection profile against evaporation rate and droplet miniaturization. For both Karnataka, shown in Fig. 10c, and New Delhi, shown in Fig. 10e, the rate of infection $\left(\mathrm{d}i^R/\mathrm{d}t\right)$ follows the rate of miniaturization of the droplets $(\mathrm{d}m^R/\mathrm{d}t)$ and these observations substantiate that the miniaturization of the *virulet* size and formation of bioaerosol directs the infection rate in the region. Fig. 10d and Fig. 10f show a good agreement of COVID–19 cases i with the evaporation rate of the droplets m for Karnataka and New Delhi. A small deviation is observed for the case of Karnataka and the same might have happened for other causes that have not been considered for the present study.

Now since the results established the faithfulness of the model for the community spreading of the infections during the waves of the pandemic, we attempt to predict the number of COVID–19 cases in the near future. For the prediction algorithm, we follow a higher order polynomial curve fitting analysis of the number of absolute cases i vs. days. The data of absolute COVID–19 cases farthest from May 2020 to June 2021 are taken as a reference for developing the polynomial fitting and the same is subsequently extrapolated for the prediction of future COVID–19 cases. The broken line portion in the plots of Fig. 10b, Fig. 10d, Fig. 10f, Fig. 10h, Fig. 10i, and Fig. 10l show the prediction data for upcoming possible COVID–19 cases. The values for the T and RH from July 2021 to

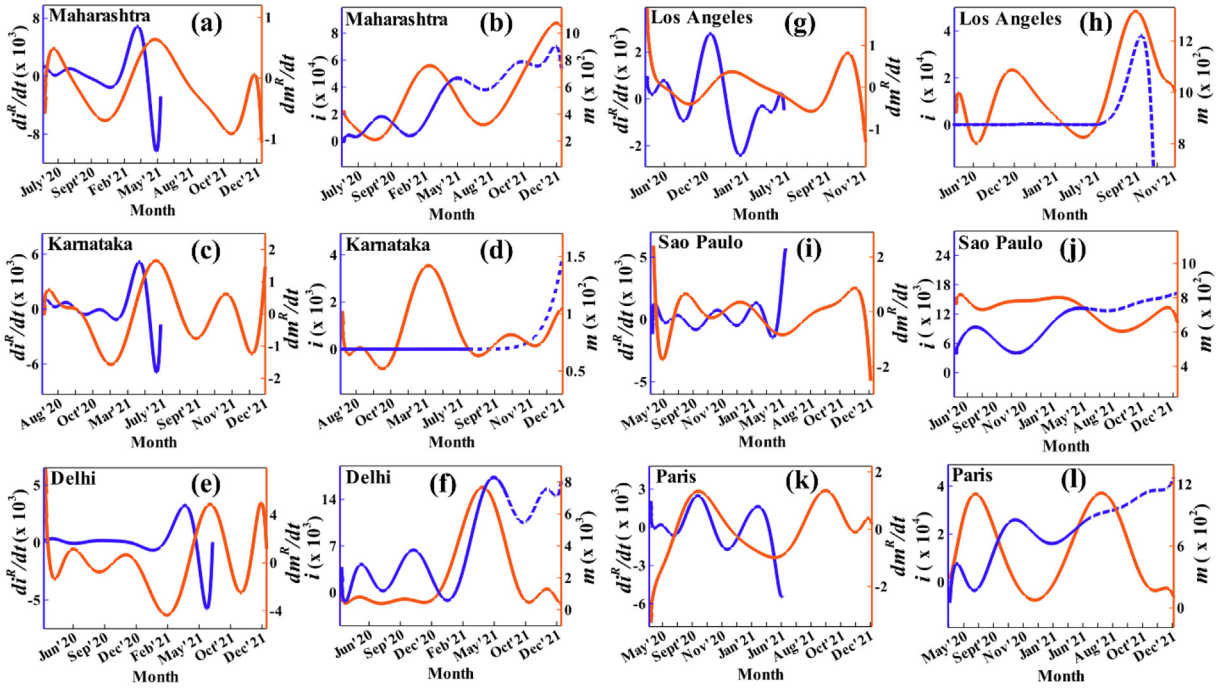

Fig. 10. Shows the comparison of rate of miniaturization $(\mathrm{d}m^R/\mathrm{d}t)$ of 100 μm sized *virulet* with the rate of change of the confirmed COVID cases $\left(\mathrm{d}i^R/\mathrm{d}t\right)$, and the evaporation rate m and confirmed cases i to predict the expected further occurrence of covid cases in near future. Subplots (a)–(f) show the trend for the three most covid affected regions in India– Maharashtra, Karnataka, and Delhi, respectively and subplots (g)–(l) show three most covid affected locations in world– Los Angeles, São Paulo, and Paris, respectively.

December 2021 are taken as an average of the last three years' data for that specific region.

We also investigate cases of three foreign cities Los Angles, São Paulo, and Paris, since the weather conditions are markedly different in the Indian cities and abroad. The plots suggest that despite a significant demographical change there is a direct correlation of the rate of infection $\left(\mathrm{d}i^R/\mathrm{d}t\right)$ with the miniaturization of the droplets $(\mathrm{d}m^R/\mathrm{d}t)$. A similar correlation is also observed for absolute infection i against the rate of evaporation m. Fig. 10g, Fig. 10i, and Fig. 10k show a comparison of the rate of infection $\left(\mathrm{d}i^R/\mathrm{d}t\right)$ with the miniaturization of the droplets $(\mathrm{d}m^R/\mathrm{d}t)$ for São Paulo, Los Angles, and Paris, respectively. These plots show a close match with occasional deflection, which may be attributed to other pandemic causes. Fig. 10h, Fig. 10j, and Fig. 10l show a correlation between the trend in the increase in COVID–19 cases i and evaporation rate m. In this absolute case analysis too, we find a close mapping between the curves.

In order to evaluate the degree of correlation between $\left(\mathrm{d}i^R/\mathrm{d}t\right)$ and $(\mathrm{d}m^R/\mathrm{d}t)$, we plotted the non-linear correlation for all the six places for the entire time period of infection. Fig. 11 shows the non-linear correlation plot for the six places. The non-linear correlation was evaluated using the non-linear estimator 'nlcor' package of the R programming language [78]. It implements a heuristic approach to evaluate the non-linear correlation between the two given parameters and returns a p-value as a factor to signify the degree of correlation. It identifies piecewise linear correlations of the local regions to estimate the overall non-linear correlation. The correlation estimate (*nlcor* value) and p-value obtained for the six selected regions are listed in Table 2. The correlation plot and Table 2 shows that the rate of infection and rate of miniaturization of the *virulets* for all six locations are significantly correlated as the p-value is less than the threshold ($p < 0.005$) [79]. Therefore, it is justified to claim that the rate of occurrence of infection cases in a particular location is also a factor of the rate of miniaturization of the ejected *virulets* driven by the geographical conditions of T and RH of the corresponding location.

Table 2
Shows the *nlcor* value and p value for the non-linear correlation of di^R/dt against dm^R/dt for the six selected places.

Location	*nlcor* value	*p*-value
Maharashtra	0.363	0.00
Karnataka	0.255	0.00
New Delhi	0.163	0.02
Los Angeles	0.401	0.00
São Paulo	0.469	0.00
Paris	0.158	0.03

The above results enlighten the role of T and RH on the evaporation driven miniaturization of the *virulets* and its significant correlation with the trend in the occurrence of the infection cases in the six different geographical locations considered in the present study. In view of that, we have done CFD simulations considering T and RH for six different places considered in the study, as shown in Fig. 12, to elucidate the transmission of the miniaturized *virulets* and to mark the optimal whether conditions that favor the maximal transmission of the *virulets* to far distances. Here, we simulated the spreading distance of the ejected *virulets* on certain weather conditions for six different places, as shown in Fig. 12.

The farther reaching *virulets* can be more potent to spread the infection to more people, however, if the *virulets* are settling at a shorter distance, the infection risk can be low but not absolutely zero. For the simulations, we kept the T of a particular region to be constant to its minimal and maximum limit and varied the RH from its lowest to the highest value, as reported on meteorological websites. In the subplots (a)–(l) of Fig. 12, the high-risk RH has been marked in red and the low-risk RH is marked in green color. If we consider the case of Maharashtra, it can be seen that for the low $T = 25^{\circ}C$, if $RH < 50\%$, the *virulets* could float in the air and reach to farther distances in less time as compared to the settling of the *virulets* as observed for $RH > 50\%$, as shown in Fig. 12(a). However, with the increase in $T = 34\ ^{\circ}\mathrm{C}$, the *virulets* could float even for larger RH, as shown in Fig. 12(b). Thus, there is a high probability that if the RH reaches lower than 50% in Maharashtra at any time of the year, there is a higher possibility of an increase in infectivity ratio.

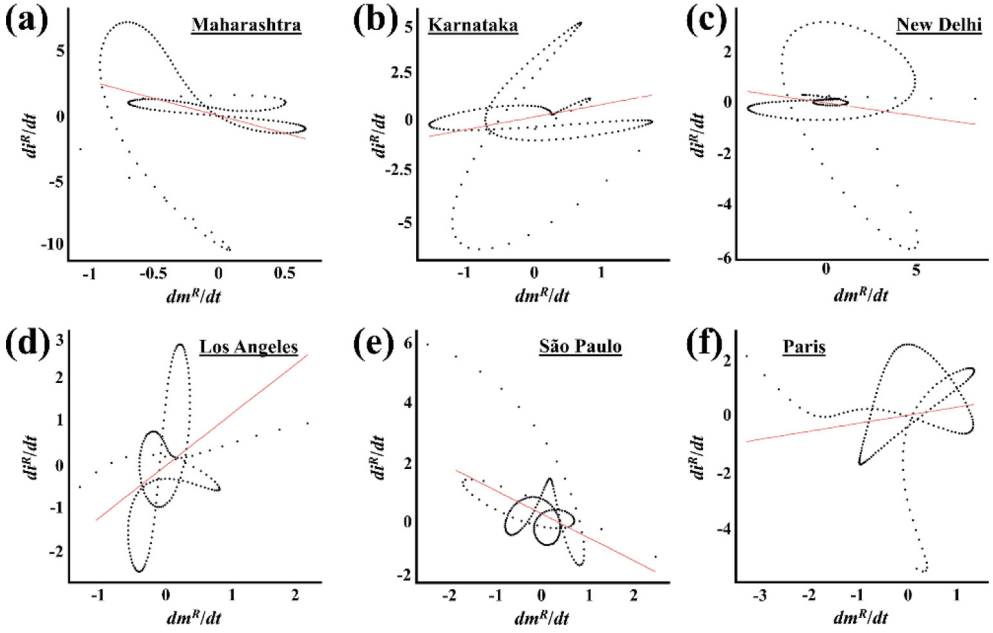

Fig. 11. Plot shows the non-linear correlation plot of di^R/dt against dm^R/dt for the six selected places.

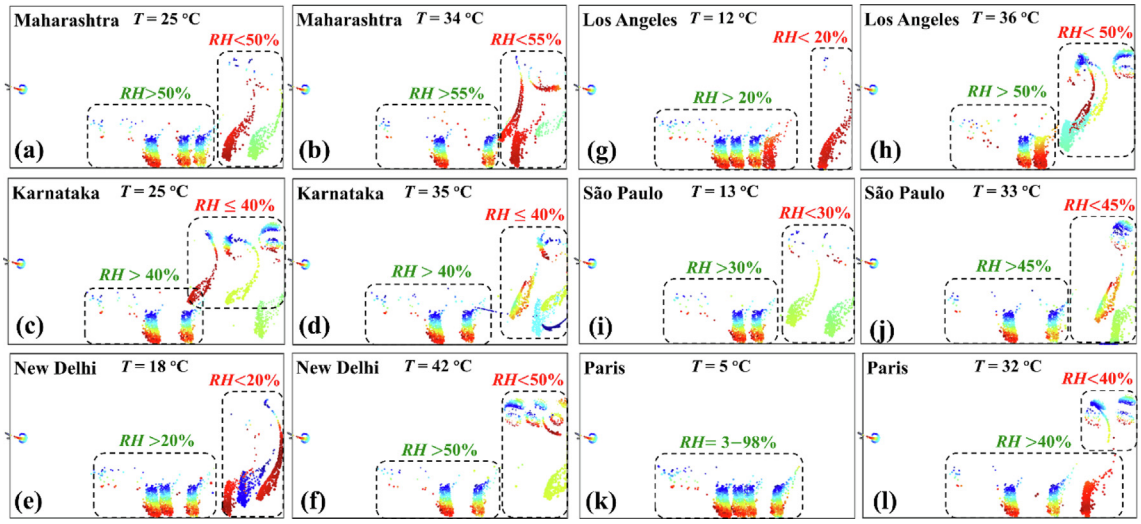

Fig. 12. The plot shows the high and low-risk weather conditions at which maximum transmission of the virulets is probable at different geographical locations.

Similarly, in Karnataka, there is a high risk of an increase in infectivity whenever the *RH* condition reaches below the semi-humid level, as shown in Fig. 12(c) and (d). Comparatively, if we consider New Delhi, the high-risk *RH* limit in colder days is found to be very lower than in warmer days, as shown in Fig. 12(d) and (e). Similarly, in Los Angeles, the high-risk *RH* limit is found to be very lower on colder days and it reaches semi-humid conditions with an increase in temperature, as shown in Fig. 12(e) and (f). In Sao Paulo, the high *RH* limit is found to vary minimally cold and warm, as shown in Fig. 12(g) and (h). In Paris, it was found that the lower the temperature, the risk level reduces which probably reduces the infectivity ratio, however, the limit increases to the semi-humid limit with an increase in temperature, as shown in Fig. 12(i) and (j).

Conclusively, it can be illustrated from all the subplots in Fig. 12 that both cold-dry and warm-semi humid conditions could be attributed to the major contributor of *virulet* miniaturization and transmission based mediator of high infectivity ratio. Though, the risk of infection transmission in other weather patterns at different geographical locations is absolutely not zero. Thus, the present work shows a satisfactory resemblance to the weather patterns for influenza flu transmission as reported in the prior studies [80,81].

Further, we have shown the authenticity of the claimed evaporation model by comparing the predicted COVID–19 infection cases (*i*, showed in the broken blue line in Fig. 10) with the reported COVID–19 infection cases (i_R) for the first and second waves of the infection in the last two years for six different geographical regions. Fig. 13 shows the match between the predicted and reported COVID–19 infection cases for the mentioned time period. It can be inferred from the figure that the trend in the occurrence of the reported infection waves in several regions matches well with the COVID–19 infection waves predicted in the present study.

Precisely, the predicted model shows exactly the same number of waves, including both weak and intense peaks, occurring at a similar time of the year as it is reported during the first and second waves of COVID-19 infection. Although, there is a lag in the intensity of the real infection cases as compared to the predicted one, which may be attributed to other additional carriers of transmission like viral seeding, population susceptibility, person-to-person contact, vaccination rate, face and mask hygiene, and others, which varies over the year and has not been added to the present study as the aim of the work is to understand the effect of *T* and *RH* only, on the miniaturization of the *virulets* and to predict its transmission with CFD study. Hence, witnessing Figs. 10–13, it is worth inferring that like with other parameters, evaporation is obviously one of the major factors in the transmission of the COVID–19 via miniaturization of the respiratory *virulets*.

Concisely, despite having multiple deciding factors for COVID community transmission, the present study unveils that *T*, *RH*, and subsequent kinetics of droplet evaporation leading to bioaerosol formation can be one of the very effective tools in predicting the future waves of a viral pandemic.

5. Conclusions

The present work compiles the various possible fluid dynamical causes of the community transmission of the highly contagious SARS–CoV–2 infection. The detailed calculations of the viral content inside the colloidal biofluid microdroplets of varying sizes, the *virulets*, ejected during the respiratory activities like sneezing and coughing gives an idea of airborne and/or droplet modes of the transmission of the disease. Further, the flow trajectories of the respiratory droplets have been simulated employing the fluid particle tracing physics, to manifest the settling distance of the *virulets* and to understand the role of bioaerosol transmission in the spreading of the disease. In relevance, it is to be mentioned that since the inception of the pandemic a few reports on droplet or bioaerosol transmission are published from last year. Most of the reported articles explore the droplet movement in the air considering only Newton's second law of motion [22,23] neglecting finer features of fluid dynamics, as described in the present study. The flow profiles of the *virulets* shown in Fig. 3 prove that the prescription of 2 m of physical distance to control the SARS–CoV–2 infections are only applicable to the large *virulets* whereas the bioaerosol is effective enough in spreading the disease to longer distances also. Furthermore, this work explicitly addresses the effect of gravity, drag, and inertial forces on the *virulets* of various sizes, which clearly explains the extent of spread of a *virulet* of interest. Likewise, the events like increased frequency of *virulet* ejection or a windy day which further enhances the spread of the disease are also discussed precisely.

Additionally, the work reveals the influence of geographical conditions on the transmission of the *virulets* at a given location. Here, the effect of *T* and *RH* has been examined [41,82,83] to measure the rate of bioaerosol generation owing to the effect of evaporation, attributed to the occurrence of the second wave of SARS–CoV–2 infection. In Fig. 10, reported infection cases of six different

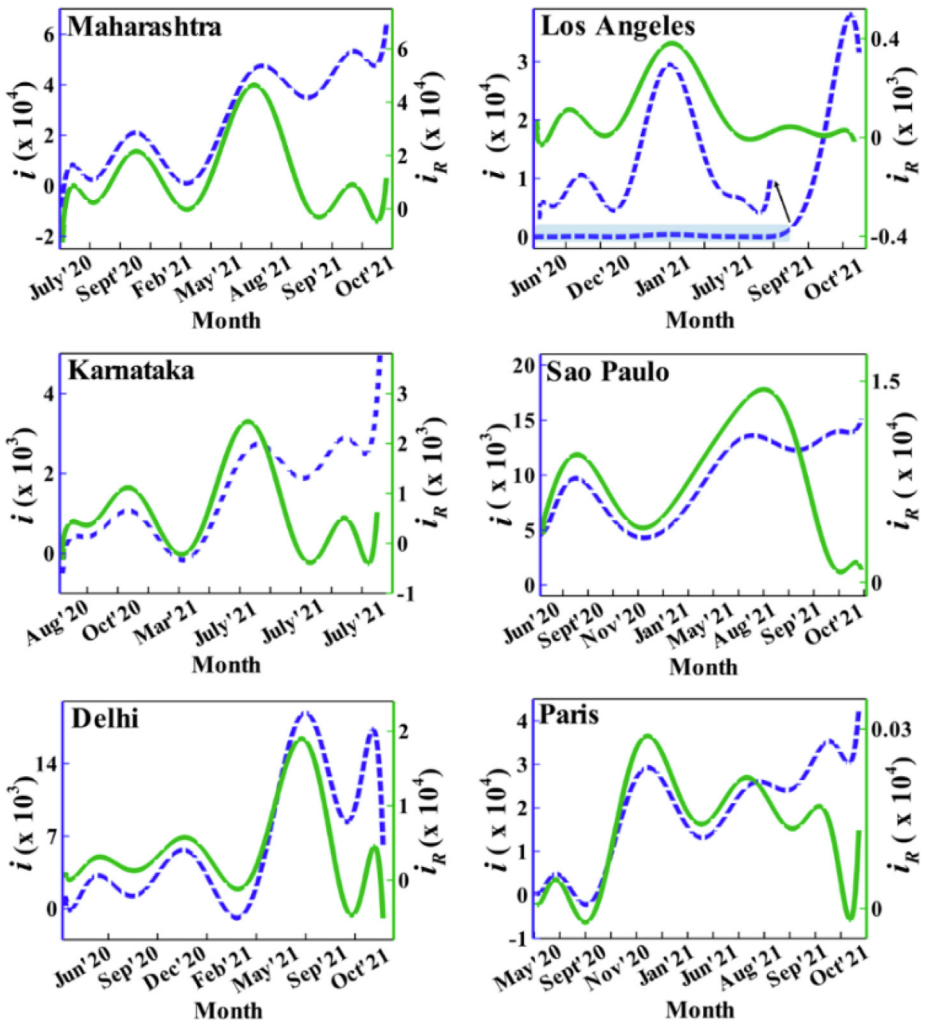

Fig. 13. Plot shows the similarity between the predicted COVID–19 infection cases (i, broken blue line) and the reported COVID–19 infection cases (i_R, solid green line). (For interpretation of the references to color in this figure legend, the reader is referred to the web version of this article.)

locations – Maharashtra, Karnataka, New Delhi, Los Angeles, São Paulo, and Paris have been mapped with the evaporation driven miniaturization rate of the *virulets* of that location for the time period of the first wave of COVID-19 infection. Interestingly, the reported infection waves show a similar trend in occurrence as that of the rate of miniaturization for a given location. To further justify the quantitative relation, in Fig. 11 and Table 2, a non-linear correlation analysis of the curves shows the *p*-value is nearly zero for all the considered locations, which proves the significant relationship between the two. The CFD studies that reported in Fig. 12 prove that both the cold-dry and warm-semi humid condition enhances the transmission of the *virulets* to long distances, attributed to the increase in infectivity ratio for that location. Importantly, the CFD simulation with varying *T* and *RH* prameters for all the cities predicted a critical *T* and *RH* value that varies from one city to another. This CFD information, can further be used for studying similar disease spreading. We extended the study to predict the future infection waves based on the *T* and *RH* mediated miniaturization of the *virulets* and later matched with the reported infection cases of the second wave of COVID-19 infection. The curves matched well in terms of frequency and time period of occurrence of the second infection wave but with a compromise of the intensity, which could be attributed to the non-consideration of various other factors of the infection at that region.

In a way, the study establishes the importance of *T* and *RH* of a given location on the spread of the infection. The study also paves the pathway to future research on explaining the most accurate method of bioaerosol formation from sneeze/cough droplets considering the various other environmental conditions and effects of elements of the colloidal microdroplets. This will also help in explaining the most realistic dynamics of bioaerosol motion and subsequent community transmission.

Mitali Basak and Shirsendu Mitra performed all of the numerical investigations, data analysis, and drafted the initial version of the manuscript. All the authors contributed in conceptualizing, writing, editing, and analyzing the results of the manuscript. The manuscript has been written through the contributions of all authors. All authors have approved the final version of the manuscript.

CRediT authorship contribution statement

Mitali Basak: Conceptualization, Methodology, Software, Investigation, Writing – original draft, Writing – review & editing, Validation, Formal analysis, Visualization. **Shirsendu Mitra:** Conceptualization, Methodology, Software, Investigation, Writing – original draft, Writing – review & editing, Validation, Formal analysis, Visualization. **Dipankar Bandyopadhyay:** Resources, Conceptualization, Methodology, Funding acquisition, Supervision, Project administration, Formal analysis, Writing – review & editing.

Declaration of Competing Interest

The authors declare that they have no known competing financial interests or personal relationships that could have appeared to influence the work reported in this paper.

Acknowledgements

We thank IIT Guwahati, MeitY – grant no. 5(9)/2012-NANO and ICMR grant no. – 5/3/8/20/2019-ITR, Government of India, for the financial supports.

Appendix A. Supplementary material

Supplementary data to this article can be found online at https://doi.org/10.1016/j.jcis.2022.03.098.

References

[1] J. Torales, M. O'Higgins, J.M. Castaldelli-Maia, A. Ventriglio, The outbreak of COVID-19 coronavirus and its impact on global mental health, Int. J. Soc. Psychiatry 66 (4) (2020) 317–320.
[2] H.A. Rothan, S.N. Byrareddy, The epidemiology and pathogenesis of coronavirus disease (COVID-19) outbreak, J. Autoimmun. 109 (2020) 102433.
[3] S.K. Gudi, K. Undela, R. Venkataraman, U.V. Mateti, M. Chhabra, S. Nyamagoud, K.K. Tiwari, Knowledge and beliefs towards universal safety precautions to flatten the curve during novel coronavirus disease (nCOVID-19) pandemic among general public in India: Explorations from a national perspective, medRxiv (2020).
[4] S. Kim, P.B. Kim, G. Lee, Predicting hospitality employees' safety performance behaviors in the COVID-19 pandemic, Int. J. Hospital. Manage. 93 (2021) 102797, https://doi.org/10.1016/j.ijhm.2020.102797.
[5] C.J. Roy, D.K. Milton, Airborne transmission of communicable infection — the elusive pathway, N Engl. J. Med. 350 (17) (2004) 1710–1712.
[6] S.A. Sattar, M.K. Ijaz, C.P. Gerba, Spread of viral infections by aerosols, Crit. Rev. Environ. Sci. Technol. 17 (2) (1987) 89–131.
[7] E. Riley, G. Murphy, R. Riley, Airborne spread of measles in a suburban elementary school, Am. J. Epidemiol. 107 (5) (1978) 421–432.
[8] Y. Liu, H.-Q. Qu, J. Qu, L. Tian, H. Hakonarson, Expression pattern of the SARS-CoV-2 entry genes ACE2 and TMPRSS2 in the respiratory tract, Viruses 12 (10) (2020) 1174.
[9] B. Scharfman, A. Techet, J. Bush, L. Bourouiba, Visualization of sneeze ejecta: steps of fluid fragmentation leading to respiratory droplets, Exp. Fluids 57 (2) (2016) 1–9.
[10] S. Yang, G.W.M. Lee, C.-M. Chen, C.-C. Wu, K.-P. Yu, The size and concentration of droplets generated by coughing in human subjects, J. Aerosol Med. 20 (4) (2007) 484–494.
[11] L. Bourouiba, Turbulent gas clouds and respiratory pathogen emissions: potential implications for reducing transmission of COVID-19, JAMA 323 (18) (2020) 1837–1838.
[12] P.D. Olch, Johann von Mikulicz-Radecki, Ann. Surg. 152 (5) (1960) 923–926.
[13] W.F. Wells, On air-borne infection. Study II. Droplets and droplet nuclei, American, J. Hygiene 20 (1934) 611–618.
[14] V. Frankova, Inhalatory infection of mice with influenza A0/PR8 virus. I. The site of primary virus replication and its spread in the respiratory tract, Acta Virol. 19 (1) (1975) 29–34.
[15] W.H. Organization, Modes of transmission of virus causing COVID-19: implications for IPC precaution recommendations: scientific brief, 27 March 2020, World Health Organization, 2020.
[16] Y.u. Feng, T. Marchal, T. Sperry, H. Yi, Influence of wind and relative humidity on the social distancing effectiveness to prevent COVID-19 airborne transmission: A numerical study, J. Aerosol Sci. 147 (2020) 105585, https://doi.org/10.1016/j.jaerosci.2020.105585.
[17] A.A. Aliabadi, S.N. Rogak, S.I. Green, K.H. Bartlett, CFD simulation of human coughs and sneezes: a study in droplet dispersion, heat, and mass transfer, ASME Int. Mech. Eng. Congr. Exposit. (2010) 1051–1060.
[18] M. Klompas, M.A. Baker, C. Rhee, Airborne transmission of SARS-CoV-2: theoretical considerations and available evidence, JAMA 324 (5) (2020) 441, https://doi.org/10.1001/jama.2020.12458.
[19] R. Bhardwaj, A. Agrawal, Likelihood of survival of coronavirus in a respiratory droplet deposited on a solid surface, Phys. Fluids 32 (6) (2020) 061704, https://doi.org/10.1063/5.0012009.
[20] J.P. Duguid, The size and the duration of air-carriage of respiratory droplets and droplet-nuclei, Epidemiol. Infect. 44 (6) (1946) 471–479.
[21] S.S. Diwan, S. Ravichandran, R. Govindarajan, R. Narasimha, Understanding transmission dynamics of COVID-19-type infections by direct numerical simulations of cough/sneeze flows, Trans. Ind. Natl. Acad. Eng. 5 (2) (2020) 255–261.
[22] T. Dbouk, D. Drikakis, On coughing and airborne droplet transmission to humans, Phys. Fluids 32 (5) (2020) 053310, https://doi.org/10.1063/5.0011960.
[23] G. Busco, S.R. Yang, J. Seo, Y.A. Hassan, Sneezing and asymptomatic virus transmission, Phys. Fluids 32 (7) (2020) 073309, https://doi.org/10.1063/5.0019090.
[24] J. Zhang, A.E. Tejada-Martínez, Q. Zhang, Developments in computational fluid dynamics-based modeling for disinfection technologies over the last two decades: a review, Environ. Modell. Software 58 (2014) 71–85.
[25] R. Wu, H. Peng, J.J. Zhu, L.P. Jiang, J. Liu, Attaching DNA to gold nanoparticles with a protein corona, Front. Chem. 25 (8) (2020 Feb) 121.
[26] J.K. Gupta, C.H. Lin, Q. Chen, Flow dynamics and characterization of a cough, Indoor Air 19 (6) (2009) 517–525.
[27] R. Mittal, R. Ni, J.-H. Seo, The flow physics of COVID-19, J. Fluid Mech. 894 (2020).
[28] W. Sun, J. Ji, Transport of droplets expelled by coughing in ventilated rooms, Indoor Built Environ. 16 (6) (2007) 493–504.
[29] J. Wei, Y. Li, Enhanced spread of expiratory droplets by turbulence in a cough jet, Build. Environ. 93 (2015) 86–96.
[30] W. Chen, N. Zhang, J. Wei, H.-L. Yen, Y. Li, Short-range airborne route dominates exposure of respiratory infection during close contact, Build. Environ. 176 (2020) 106859.
[31] M. Mirzaie, E. Lakzian, A. Khan, M.E. Warkiani, O. Mahian, G. Ahmadi, COVID-19 spread in a classroom equipped with partition–A CFD approach, J. Hazard. Mater. 420 (2021) 126587.
[32] S. Shao, D. Zhou, R. He, J. Li, S. Zou, K. Mallery, S. Kumar, S. Yang, J. Hong, Risk assessment of airborne transmission of COVID-19 by asymptomatic individuals under different practical settings, J. Aerosol Sci. 151 (2021) 105661.
[33] Y. Zhang, G. Feng, Y. Bi, Y. Cai, Z. Zhang, G. Cao, Distribution of droplet aerosols generated by mouth coughing and nose breathing in an air-conditioned room, Sustain. Cities Soc. 51 (2019) 101721.
[34] B. Zhao, Z. Zhang, X. Li, Numerical study of the transport of droplets or particles generated by respiratory system indoors, Build. Environ. 40 (8) (2005) 1032–1039.
[35] C. Crawford, E. Vanoli, B. Decorde, M. Lancelot, C. Duprat, C. Josserand, J. Jilesen, L. Bouadma, J.-F. Timsit, Modeling of aerosol transmission of airborne pathogens in ICU rooms of COVID-19 patients with acute respiratory failure, Sci. Rep. 11 (1) (2021) 1–12.
[36] E. Conticini, B. Frediani, D. Caro, Can atmospheric pollution be considered a co-factor in extremely high level of SARS-CoV-2 lethality in Northern Italy?, Environ Pollut. 261 (2020) 114465, https://doi.org/10.1016/j.envpol.2020.114465.
[37] Mariam, A. Magar, M. Joshi, P.S. Rajagopal, A. Khan, M.M. Rao, B.K. Sapra, CFD Simulation of the Airborne Transmission of COVID-19 Vectors Emitted during Respiratory Mechanisms: Revisiting the Concept of Safe Distance, ACS, Omega 6 (26) (2021) 16876–16889.
[38] S. Basu, P. Kabi, S. Chaudhuri, A. Saha, Insights on drying and precipitation dynamics of respiratory droplets from the perspective of COVID-19, Phys. Fluids 32 (12) (2020) 123317, https://doi.org/10.1063/5.0037360.
[39] S. Chaudhuri, S. Basu, P. Kabi, V.R. Unni, A. Saha, Modeling the role of respiratory droplets in Covid-19 type pandemics, Phys. Fluids 32 (6) (2020) 063309, https://doi.org/10.1063/5.0015984.
[40] J. Wang, M. Alipour, G. Soligo, A. Roccon, M. De Paoli, F. Picano, A. Soldati, Short-range exposure to airborne virus transmission and current guidelines, medRxiv (2021).
[41] R.R. Netz, Mechanisms of airborne infection via evaporating and sedimenting droplets produced by speaking, J. Phys. Chem. B 124 (33) (2020) 7093–7101.
[42] E. Bormashenko, A.A. Fedorets, L.A. Dombrovsky, M. Nosonovsky, Survival of virus particles in water droplets: hydrophobic forces and Landauer's principle, Entropy 23 (2) (2021) 181.
[43] L.A. Dombrovsky, A.A. Fedorets, V.Y. Levashov, A.P. Kryukov, E. Bormashenko, M. Nosonovsky, Modeling evaporation of water droplets as applied to survival of airborne viruses, Atmosphere 11 (9) (2020) 965.
[44] M.-R. Pendar, J.C. Páscoa, Numerical modeling of the distribution of virus carrying saliva droplets during sneeze and cough, Phys. Fluids 32 (8) (2020) 083305, https://doi.org/10.1063/5.0018432.
[45] L. Zhao, Y. Qi, P. Luzzatto-Fegiz, Y. Cui, Y. Zhu, COVID-19: effects of environmental conditions on the propagation of respiratory droplets, Nano Lett. 20 (10) (2020) 7744–7750.
[46] C.C. Wang, K.A. Prather, J. Sznitman, J.L. Jimenez, S.S. Lakdawala, Z. Tufekci, L.C. Marr, Airborne transmission of respiratory viruses, Science 373 (6558) (2021) eabd9149.
[47] C. Ranjan, nlcor: Compute Nonlinear Correlations, ProcessMiner Inc., Atlanta, GA, USA, 2020.
[48] H. Nishimura, S. Sakata, A. Kaga, K. Harrod, A new methodology for studying dynamics of aerosol particles in sneeze and cough using a digital high-vision, high-speed video system and vector analyses, PLoS One 8 (11) (2013) e80244.
[49] S. Bhattacharyya, S. Dhinakaran, A. Khalili, Fluid motion around and through a porous cylinder, Chem. Eng. Sci. 61 (13) (2006) 4451–4461.
[50] C. Bonadonna, G.G.J. Ernst, R.S.J. Sparks, Thickness variations and volume estimates of tephra fall deposits: the importance of particle Reynolds number, J. Volcanol. Geoth. Res. 81 (3-4) (1998) 173–187.
[51] Y. Pan, D. Zhang, P. Yang, L.L.M. Poon, Q. Wang, Viral load of SARS-CoV-2 in clinical samples, Lancet. Infect. Dis 20 (4) (2020) 411–412.

[52] S. Anand, Y. Mayya, Size distribution of virus laden droplets from expiratory ejecta of infected subjects, Sci. Rep. 10 (1) (2020) 1–9.
[53] C. Liu, L. Mendonça, Y. Yang, Y. Gao, C. Shen, J. Liu, T. Ni, B. Ju, C. Liu, X. Tang, J. Wei, X. Ma, Y. Zhu, W. Liu, S. Xu, Y. Liu, J. Yuan, J. Wu, Z. Liu, Z. Zhang, L. Liu, P. Wang, P. Zhang, The Architecture of Inactivated SARS-CoV-2 with Postfusion Spikes Revealed by Cryo-EM and Cryo-ET, Structure 28 (11) (2020) 1218–1224.e4.
[54] P. Bahl, C.M. de Silva, A.A. Chughtai, C.R. MacIntyre, C. Doolan, An experimental framework to capture the flow dynamics of droplets expelled by a sneeze, Exp. Fluids 61 (8) (2020) 1–9.
[55] R. Plamondon, S.N. Srihari, Online and off-line handwriting recognition: a comprehensive survey, IEEE Trans. Pattern Anal. Mach. Intell. 22 (1) (2000) 63–84.
[56] A.H. Shafaghi, F. Rokhsar Talabazar, A. Koşar, M. Ghorbani, On the Effect of the Respiratory Droplet Generation Condition on COVID-19 Transmission, Fluids 5 (3) (2020) 113.
[57] Z. Sun, H. Zhang, Y. Yang, H. Wan, Y. Wang, Impacts of geographic factors and population density on the COVID-19 spreading under the lockdown policies of China, Sci. Total Environ. 746 (2020) 141347.
[58] J. Zhao, Y. Yang, H. Huang, D. Li, D. Gu, X. Lu, Z. Zhang, L. Liu, T. Liu, Y. Liu, Relationship between the ABO blood group and the coronavirus disease 2019 (COVID-19) susceptibility, Clin. Infect. Dis. 73(2) (2021) 328–331.
[59] T.P. Velavan, C.G. Meyer, The COVID-19 epidemic, Trop. Med. Int. Health 25 (3) (2020) 278–280.
[60] N. Chen, M. Zhou, X. Dong, J. Qu, F. Gong, Y. Han, Y. Qiu, J. Wang, Y. Liu, Y. Wei, Epidemiological and clinical characteristics of 99 cases of 2019 novel coronavirus pneumonia in Wuhan, China: a descriptive study, The lancet 395 (10223) (2020) 507–513.
[61] A. Kumar, K.R. Nayar, S.F. Koya, COVID-19: Challenges and its consequences for rural health care in India, Public Health Pract. 1 (2020) 100009.
[62] B.B. Finlay, K.R. Amato, M. Azad, M.J. Blaser, T.C.G. Bosch, H. Chu, M.G. Dominguez-Bello, S.D. Ehrlich, E. Elinav, N. Geva-Zatorsky, P. Gros, K. Guillemin, F. Keck, T. Korem, M.J. McFall-Ngai, M.K. Melby, M. Nichter, S. Pettersson, H. Poinar, T. Rees, C. Tropini, L. Zhao, T. Giles-Vernick, The hygiene hypothesis, the COVID pandemic, Proc. Natl. Acad. Sci. USA 118 (6) (2021), https://doi.org/10.1073/pnas.2010217118.
[63] O. Abu-Hammad, A. Alnazzawi, S. Borzangy, A. Abu-Hammad, M. Fayad, S. Saadaledin, S. Abu-Hammad, N. Dar-Odeh, Factors influencing global variations in COVID-19 cases and fatalities; a review, in: Healthcare, Multidisciplinary Digital Publishing Institute, 2020, p. 216, https://doi.org/10.3390/healthcare8030216.
[64] K.J. Godri Pollitt, J. Peccia, A.I. Ko, N. Kaminski, C.S. Dela Cruz, D.W. Nebert, J.K. Reichardt, D.C. Thompson, V. Vasiliou, COVID-19 vulnerability: the potential impact of genetic susceptibility and airborne transmission, Human Genomics 14 (2020) 1–7.
[65] M.S. Islam, K.M. Rahman, Y. Sun, M.O. Qureshi, I. Abdi, A.A. Chughtai, H. Seale, Current knowledge of COVID-19 and infection prevention and control strategies in healthcare settings: A global analysis, Infect. Control Hosp. Epidemiol. 41 (10) (2020) 1196–1206.
[66] J. Liu, J.i. Zhou, J. Yao, X. Zhang, L. Li, X. Xu, X. He, B.o. Wang, S. Fu, T. Niu, J. Yan, Y. Shi, X. Ren, J. Niu, W. Zhu, S. Li, B. Luo, K. Zhang, Impact of meteorological factors on the COVID-19 transmission: A multi-city study in China, Sci. Total Environ. 726 (2020) 138513, https://doi.org/10.1016/j.scitotenv.2020.138513.
[67] A.A. Dawood, Mutated COVID-19 may foretell a great risk for mankind in the future, New Microbes New Infect. 35 (2020) 100673.
[68] T.N. Vilches, K. Zhang, R. Van Exan, J.M. Langley, S.M. Moghadas, Projecting the impact of a two-dose COVID-19 vaccination campaign in Ontario, Canada, Vaccine 39 (17) (2021) 2360–2365.
[69] L. Comber, E. O Murchu, L. Drummond, P.G. Carty, K.A. Walsh, C.F. De Gascun, M.A. Connolly, S.M. Smith, M. O'Neill, M. Ryan, P. Harrington, Airborne transmission of SARS-CoV-2 via aerosols, Rev. Med. Virol. 31 (3) (2021), https://doi.org/10.1002/rmv.v31.310.1002/rmv.2184.
[70] A. Robotto, P. Quaglino, D. Lembo, M. Morello, E. Brizio, L. Bardi, A. Civra, SARS-CoV-2 and indoor/outdoor air samples: a methodological approach to have consistent and comparable results, Environ. Res. 195 (2021) 110847.
[71] A.L. Katelaris, J. Wells, P. Clark, S. Norton, R. Rockett, A. Arnott, V. Sintchenko, S. Corbett, S.K. Bag, Epidemiologic evidence for airborne transmission of SARS-CoV-2 during church singing, Australia, 2020, Emerg. Infect. Dis. 27 (6) (2021) 1677–1680.
[72] E. Crema, The SARS-COV-2 outbreak around the Amazon rainforest: The relevance of the airborne transmission, Sci. Total Environ. 759 (2021) 144312.
[73] A.D. Langmuir, PART I. Keynote address: epidemiology of airborne infection, Bacteriol. Rev. 25 (3) (1961) 173–181.
[74] R.E. Williams, Epidemiology of airborne staphylococcal infection, Bacteriol. Rev. 30 (3) (1966) 660–674.
[75] C.F. Dillon, M.B. Dillon, H.L. Drake, Multiscale Airborne Infectious Disease Transmission, Appl. Environ. Microbiol. 87 (4) (2021), https://doi.org/10.1128/AEM.02314-20.
[76] O. Mohr, M. Askar, S. Schink, T. Eckmanns, G. Krause, G. Poggensee, Evidence for airborne infectious disease transmission in public ground transport–a literature review, Eurosurveillance 17 (35) (2012) 20255.
[77] R.E. Williamson, E.D. Threadgill, A simulation for the dynamics of evaporating spray droplets in agricultural spraying, Trans. ASAE 17 (2) (1974) 254–0261.
[78] Ranjan, C., Najari, V., 2019. https://rdrr.io/github/ProcessMiner/nlcor/f/README.md.
[79] O.E. Hart, R.U. Halden, Simulated 2017 nationwide sampling at 13,940 major US sewage treatment plants to assess seasonal population bias in wastewater-based epidemiology, Sci. Total Environ. 727 (2020) 138406.
[80] J.D. Tamerius, J. Shaman, W.J. Alonso, K. Bloom-Feshbach, C.K. Uejio, A. Comrie, C. Viboud, S. Riley, Environmental predictors of seasonal influenza epidemics across temperate and tropical climates, PLoS Pathog. 9 (3) (2013) e1003194.
[81] H. Foster, The Reason for the Season: Why Flu Strikes in Winter, Blog post. Harvard University, The Graduate School of Arts and Sciences website, 2014.
[82] J. Wang, M. Alipour, G. Soligo, A. Roccon, M. De Paoli, F. Picano, A.J.m. Soldati, Short-range exposure to airborne virus transmission and current guidelines, (2021).
[83] Y. Feng, T. Marchal, T. Sperry, H. Yi, Influence of wind and relative humidity on the social distancing effectiveness to prevent COVID-19 airborne transmission: A numerical study, J. Aerosol Sci. 1 (147) (2020).